The Astrophysical Journal, 893:34 (19pp), 2020 April 10 https://doi.org/10.3847/1538-4357/ab8010

Plasma Diagnostics from Active Region and Quiet-Sun Spectra Observed by Hinode/EIS: Quantifying the Departures from a Maxwellian Distribution

Juraj Lörinčík[1,2], Jaroslav Dudík[2], Giulio del Zanna[3], Elena Dzifčáková[2], and Helen E. Mason[3]
[1] Institute of Astronomy, Charles University, V Holešovičkách 2, CZ-18000 Prague 8, Czech Republic; juraj.lorincik@asu.cas.cz
[2] Astronomical Institute of the Czech Academy of Sciences, Fričova 298, 251 65 Ondřejov, Czech Republic
[3] DAMTP, Centre for Mathematical Sciences, Wilberforce Road, Cambridge, CB3 OWA, UK
Received 2020 January 7; revised 2020 March 3; accepted 2020 March 14; published 2020 April 14

Abstract

We perform plasma diagnostics, including that of the non-Maxwellian κ-distributions, in several structures observed in the solar corona by the Extreme-Ultraviolet Imaging Spectrometer (EIS) on board the Hinode spacecraft. To prevent uncertainties due to the in-flight calibration of EIS, we selected spectral atlases observed shortly after the launch of the mission. One spectral atlas contains an observation of an active region, while the other is an off-limb quiet-Sun region. To minimize the uncertainties of the diagnostics, we rely only on strong lines and average the signal over a spatial area within selected structures. Multiple plasma parameters are diagnosed, such as the electron density, the differential emission measure, and the non-Maxwellian parameter κ. To do that, we use a simple, well-converging iterative scheme based on refining the initial density estimates via the differential emission measure (DEM) and κ. We find that while the quiet-Sun spectra are consistent with a Maxwellian distribution, the coronal loops and moss observed within the active region are strongly non-Maxwellian with $\kappa \lessapprox 3$. These results were checked by calculating synthetic ratios using DEMs obtained as a function of κ. Ratios predicted using the DEMs assuming κ-distributions converged to the ratios observed in the quiet Sun and coronal loops. To our knowledge, this work presents a strong evidence of the presence of different electron distributions between two physically distinct parts of the solar corona.

Unified Astronomy Thesaurus concepts: Solar corona (1483); Solar extreme ultraviolet emission (1493); Spectroscopy (1558); Non-thermal radiation sources (1119)

1. Introduction

Dynamic phenomena that take place in the solar atmosphere can violate plasma equilibrium, leading to non-Maxwellian (nonthermal) distributions of particles. Populations of non-Maxwellian particles are expected to be present in different parts and structures of the solar atmosphere, where acceleration mechanisms such as turbulence, shocks, and magnetic reconnection are likely to occur (see Dudík et al. 2017, and references therein). The most prominent among these are probably the solar flares, releasing enormous amounts of nonthermal electrons accelerated to speeds reaching fractions of c (see, e.g., Fletcher et al. 2011; Bian et al. 2014; Oka et al. 2018). A typical example of the nonthermal emission is observed, e.g., in the form of power laws in X-ray spectra of instruments such as RHESSI or recently NuSTAR. It usually originates in bremsstrahlung and microflares (e.g., Christe et al. 2008; Hannah et al. 2008; Wright et al. 2017), whose energy outputs are lower compared to those of solar flares (e.g., Lin et al. 1984). Nonthermal electrons are also predicted to accompany nanoflares (Bakke et al. 2018; Che 2018), nowadays commonly discussed in terms of coronal heating (see, e.g., Klimchuk 2006; Reep et al. 2013; Viall & Klimchuk 2017; Priest et al. 2018).

An example of a non-Maxwellian distribution of particle energies or velocities is the κ (kappa) distribution. This is defined as (e.g., Owocki & Scudder 1983; Livadiotis 2017)

$$f_\kappa(E) = \left(\frac{m}{2\pi k_B T}\right)^{3/2} \frac{A_\kappa}{\left(1 + \frac{E}{(\kappa - 3/2) k_B T}\right)^{\kappa+1}}, \quad (1)$$

where A_κ is a normalization constant $\Gamma(\kappa + 1)/[\Gamma(\kappa - 1/2)(\kappa - 3/2)^{3/2}]$, k_B is Boltzmann's constant, and m is the electron mass. The distribution has two parameters: temperature $T \in (0, \infty)$ for which the physical meaning is the same as that of the kinetic temperature T in the Maxwellian distribution (Livadiotis & McComas 2009), and $\kappa \in (3/2, \infty)$, which describes the system's departure from the Maxwellian. $\kappa \to \infty$ corresponds to the Maxwellian distribution, while $\kappa \to 3/2$ describes its furthest departure. The κ-distributions are characterized by a nearly Maxwellian core and a suprathermal tail. The fraction of particles corresponding to this tail can, e.g., in the case of the $\kappa = 2$ distribution, contain more than 80% of the total energy of electrons in the system (Oka et al. 2013).

The κ-distributions, or distributions with enhanced high-energy tail, are expected to occur owing to a range of processes, such as acceleration due to electric fields (e.g., Burge et al. 2012; Gordovskyy et al. 2013, 2014; Ripperda et al. 2017; Threlfall et al. 2018), turbulence (Hasegawa et al. 1985; Laming & Lepri 2007; Bian et al. 2014; Che & Goldstein 2014), wave–particle interactions (Vocks et al. 2008, 2016), and density or temperature gradients (Roussel-Dupré 1980; Shoub 1983; Ljepojevic & MacNeice 1988). More generally, they occur wherever the Knudsen number is larger than about 0.01 (Scudder 2019), a condition commonly expected in solar and stellar coronae (Scudder & Karimabadi 2013).

The κ-distributions have an influence on the ionization equilibrium (Dzifčáková 1992; Wannawichian et al. 2003; Dzifčáková & Dudík 2013) and excitation rates (e.g., Dzifčáková 2006; Dzifčáková & Mason 2008) and affect other processes and quantities (e.g., Marsch 2006; de Avillez & Breitschwerdt 2015;

Lazar et al. 2016; Livadiotis 2017; Meyer-Vernet et al. 2017; de Avillez et al. 2018, and references therein). Therefore, the κ-distributions alter relative intensities of spectral lines in an optically thin plasma. Details of the spectral synthesis using the original excitation cross sections for iron ions can be found in Dudík et al. (2014). Approximations of the excitation cross sections for all astrophysically relevant ions, based on modifications of the rates as available in the CHIANTI v7.1 database (Dere et al. 1997; Landi et al. 2013), are contained in the KAPPA package (Dzifčáková et al. 2015).

The first discovery of a κ-distribution was obtained from in situ measurements of electron velocities in Earth's magnetosphere (Olbert 1968; Vasyliunas 1968) and later on in the solar wind (e.g., Maksimovic et al. 1997; Nieves-Chinchilla & Viñas 2008; Le Chat et al. 2010; Martinović et al. 2016). Ever since, distributions of particles with suprathermal tails have been detected in various kinds of space plasmas (see, e.g., the review of Pierrard & Lazar 2010). A question thus arises whether the non-Maxwellians in solar wind indeed originate in the solar corona. The presence of κ-distributions of ions is manifested in broad profiles of emission lines formed, e.g., in flare conditions (Jeffrey et al. 2016, 2017; Polito et al. 2018), which authors fitted with κ as low as 2. Comparable values of κ were used by Dudík et al. (2017) to fit lines of Si IV, O IV, and S IV observed by the Interface Region Imaging Spectrograph in the center of the studied active region (AR). Furthermore, Dzifčáková et al. (2017) found that high-energy tails indeed significantly affect these transition region lines. Electron κ-distributions can be investigated in two ways: first by the direct fitting of high-energy tails of HXR spectra (Kašparová & Karlický 2009; Oka et al. 2013, 2015, 2018), and then by using ratios of line intensities.

A method for diagnostics of κ utilizing ratios of line intensities was developed by Dzifčáková & Kulinová (2010). It is based on comparing observed and theoretical line intensity ratios, one sensitive to T and the other to κ, plotted on both axes of the ratio–ratio diagrams constructed for known densities. Since we use this method in this manuscript, it is further described in Section 3.2.3.

Theoretical combinations of line ratios sensitive to κ observed by the Extreme-ultraviolet and Imaging Spectrometer (EIS; Culhane et al. 2007) on board the Hinode satellite (Kosugi et al. 2007) were investigated by Dzifčáková & Kulinová (2010) and Dudík et al. (2014, 2019). In all cases, one line in a ratio sensitive to κ is observed in the short-wavelength channel and the other in the long-wavelength channel. Measurements of the parameter κ using the ratio–ratio diagrams in the solar corona were performed by Mackovjak et al. (2013) and Dudík et al. (2015) using data observed by EIS. Mackovjak et al. (2013) attempted to diagnose the electron distributions using lines of oxygen and sulfur but were unable to precisely measure the parameter κ because some lines were weak, or unresolved blends were present, both issues leading to large uncertainties. Dudík et al. (2015) used multiple ratios of Fe line intensities to find extremely non-Maxwellian distributions with $\kappa \leqslant 2$ in a transient coronal loop. The authors also accounted for the multithermal effects in the observed plasma. The observed ratios were found to be reproduced best by synthetic ratios calculated for the $\kappa = 2$ distribution. Finally, Dzifčáková et al. (2018) applied the ratio–ratio method to flare spectra observed by the Extreme-Ultraviolet Variability Experiment (EVE; Woods et al. 2012) on board the Solar Dynamics Observatory. The authors showed that plasma is strongly non-Maxwellian with $\kappa \leqslant 2$ during the early and impulsive phases of the flare and thermalizes in the gradual phase.

As we mentioned before, the ratio–ratio technique for diagnostics of κ works for known electron densities. Therefore, the electron densities need to be determined before the diagnostics of κ can be applied. Mackovjak et al. (2013) and Dudík et al. (2015) did so by using measurements of density-sensitive line intensity ratios. These ratios are, however, also slightly sensitive to both T and κ, and as a result, the authors were only able to constrain the range of possible densities, which for some structures were as large as 0.8 dex in $\log(N_e\,[\mathrm{cm}^{-3}])$. Since the measurements of κ are dependent on the electron density, this increases the uncertainties in the diagnostics.

Furthermore, Dudík et al. (2015) discussed the EIS calibration and its degradation as another possible source of uncertainties. Since the launch of Hinode in 2006, there have been several studies quantifying the changes in the in-flight calibration, in particular the decrease of sensitivity of the long-wavelength channel of EIS compared to the short-wavelength one (e.g., Del Zanna 2013a; Mariska 2013; Warren et al. 2014). Two in-flight calibration routines were developed to revise the effective areas and account for the sensitivity decay with time (Del Zanna 2013a; Warren et al. 2014). As either of these routines has strong effects on several diagnostic ratios, the uncertainties in the previous results are considerable.

In this work, we present the measurements of plasma from data sets obtained soon after the launch of Hinode taken near in time, to reduce problems with the degradation of sensitivity. Furthermore, the diagnostics of κ is here coupled with accurate measurements of the electron density. This manuscript is organized as follows. In Section 2 we describe the observations and the data reduction. Section 3 outlines the diagnostic methods used for measurements of plasma parameters. We employ an iterative method (Section 3.2) that significantly decreases the uncertainties in the measurements of the electron density (Section 3.2.1), coupled with diagnostics of the differential emission measure (DEM; Section 3.2.2), as well as temperature and κ (Section 3.2.3). The results are presented in Section 4. In Section 5, a discussion of the results is provided. Finally, our findings are summarized in Section 6.

2. Hinode/EIS Observations of the Active Region and Quiet Sun

To analyze plasma properties in different regions within the solar corona, we used data containing observations of an AR and quiet Sun (QS) observed by Hinode/EIS. To carry out this study, we use the spectral atlases, i.e., observations in which the whole spectral range of the instrument is observed.

We have selected observations of NOAA Active Region 10940 observed on 2007 February 5. This AR was rastered from 10:52:12 UT in 30 s exposures using a 1″ slit. The spectral atlas containing observations of an off-limb QS was rastered on 2007 March 11. The observations were carried out using 1″ slit and 90 s exposures and started at 02:32:12 UT.

The observations of the AR are shown in Figures 1 and 2, while the QS observations are shown in Figure 3. To have an overview of the temperature structure of the regions observed, Figures 1 and 2 show EIS spectral lines of ions formed at different temperatures. To obtain these images, the selected spectral lines were fitted in the whole EIS field of view (FOV)

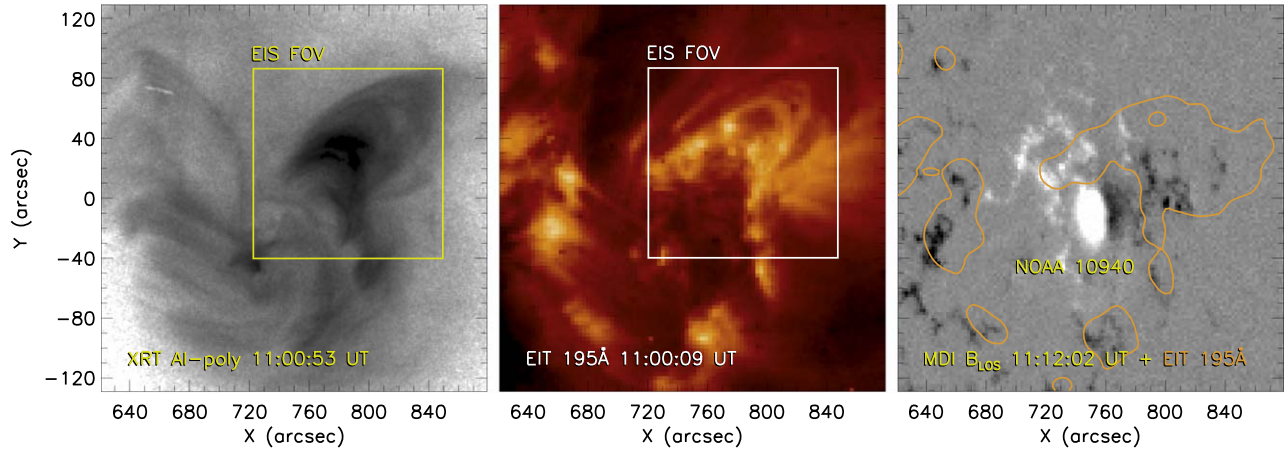

Figure 1. Context observations of NOAA AR 10940 observed in the Al-poly filter channel of XRT (left) and 195 Å filter channel of EIT (middle). The FOV of EIS is indicated using yellow and white frames. The right panel shows the MDI magnetogram overlaid with contours corresponding to 5 DN s^{-1} pixel^{-1} in the 195 Å channel of EIT.

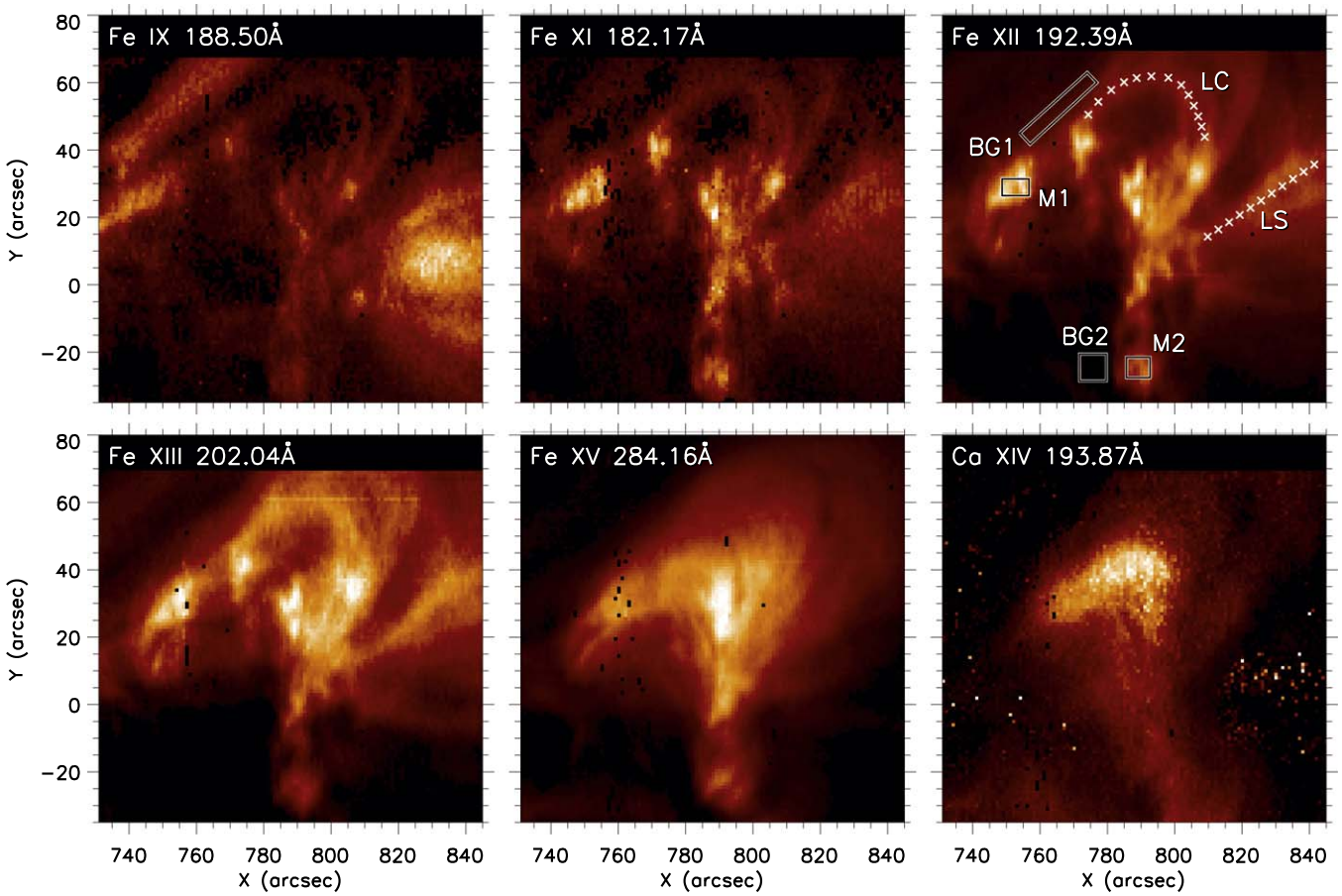

Figure 2. Context observations of NOAA AR 10940 observed on 2007 February 5 in different spectral lines observed by EIS. Acronyms shown in the Fe XII λ192.39 line mark structures in which we have averaged intensities and used for later diagnostics of the plasma.

using the automatic fitting routine `auto_fit`. Where applicable, multi-Gaussian fits were used to fit the observed spectra.

Note that an extensive discussion on the temperature structure of the observed plasma is left to Sections 4.2 and 4.3.

2.1. Data Reduction

Both spectral atlases were processed in the same manner. Data were first converted into level 1 using the `eis_prep` routine. The correction for spectrum rotation was then applied, with *Y*-offsets found using the standard `eis_ccd_offset` procedure. We then had to shift the data in the long-wavelength channel by 2″ in *X* because of their relative shift with respect to the short-wavelength channel data. We also found that the raster steps in solar *X* are not equal to the slit width of 1″ (see Del Zanna et al. 2011). However, since we perform diagnostics from EIS measurements only, these small

inconsistencies, below the spatial resolution of EIS, were neglected.

Both AR and QS data sets contained less than 1% of missing pixels, which we excluded from the statistics. Most of them were visible at wavelengths of about 193 Å and were located at certain positions along the slit, at approximately $Y \approx 690''$ in the QS data and $Y \approx 0''$ in the AR data.

Since both data sets were observed relatively shortly after the launch of the instrument, we used the ground calibration (Culhane et al. 2007) for the absolute calibration of intensities. The data were not corrected further for degradation. Any such degradation in early 2007 would be only a few percent (see Figure 9 in Del Zanna 2013a).

2.2. AR Observations

2.2.1. Context Observations

Since EIS observed only a portion of NOAA AR 10940, we first examined the context observations provided by other instruments taken at the same time as the EIS observations. The X-ray Telescope (XRT; Golub et al. 2007) was imaging the AR mainly in the Al-poly channel. Data were processed using the standard routines `xrt_prep`, `xrt_jitter` and then manually co-aligned with EIS using lines formed at temperatures corresponding to the AR core. The XRT image, shown in the left panel of Figure 1, reveals the bright core of the AR, an arcade of the AR loops, and fainter loops rooted on the eastern and southern side of the FOV. The EIS FOV is indicated by the yellow box.

We also examined imaging data produced by the instruments on board the Solar and Heliospheric Observatory (SOHO). The Extreme ultraviolet Imaging Telescope (EIT; Delaboudinière et al. 1995) observed this AR in the 195 Å filter channel at a cadence of 12 minutes. EIT data were then manually co-aligned with the Fe XII λ195.12 intensities observed by EIS and are shown in the middle panel of Figure 1. Upon inspection of the EIT data, we did not find any significant changes in the morphology of the AR during the period of the EIS rastering. In particular, no major brightenings occurred within the AR, which is also supported by the flat light curve of the GOES X-ray flux during the period studied (not shown).

The magnetic structure of the AR was examined using the $B_{\rm LOS}$ data measured by the Michelson Doppler Imager (MDI; Scherrer et al. 1995) on board SOHO. The right panel of Figure 1 shows level 1.8 MDI data saturated to $\pm$1000 G, co-aligned with EIT. To compare the morphology of the AR with the distribution of the underlying magnetic field, we overplotted the $B_{\rm LOS}$ data with 195 Å filter channel contours (orange) corresponding to 5 DN s^{-1} pixel^{-1} produced using data smoothed by a 5 $\times$ 5 boxcar.

2.2.2. Observations of the Active Region

Figure 2 shows that in the lines of Fe XI–Fe XIII, which are primarily used for diagnostics, as well as in other lines, the observed AR is structured. Relatively short AR loops are present, together with long loops overlying the AR, as well as coronal moss located at the footpoints of the hot core emission.

In the Fe IX λ188.50 and Fe XI λ182.17 ($\log T_{\rm max}$ [K] = 6.15) line images, we see short and relatively faint AR loops located at about [800″, 50″]. At ≈[830″, 0″], lower portions of long and bright coronal loops overlying the AR are visible. Conjugate footpoints of these loops are distributed in several patches, one of which can be seen at ≈[740″, 40″], while the other ones are outside of the EIS FOV. The coronal moss is located at the footpoints of hot core loops, for example, in a small bright region at ≈[740″, 20″] and in an elongated region located at $X \approx 790''$.

The structure of the AR is similar in the Fe XII λ192.39 and Fe XIII λ202.04 line images. The short AR loops seen in Fe IX and Fe XI belong to a bright arcade, a portion of which is beyond the EIS FOV. One of these loops, hereinafter referred to as the "curved loop" ("LC"), is in the Fe XII λ192.39 image highlighted with crosses. We selected this loop for further diagnostics. Note that this loop can be split into several strands in cooler lines.

Furthermore, there is a fainter, broad bundle of long fan loops rooted on the western side of the AR. We selected one relatively bright loop for further diagnostics, and in the remainder of this paper we will refer to it as the "straight loop" ("LS"; see Figure 2).

Observations in hotter spectral lines, such as the Fe XV λ284.16 line ($\log(T_{\rm max}$ [K]) = 6.35 for Maxwellian conditions), reveal typical thermal structure of the AR, with hot emission concentrated in the core. In the "hottest line" shown in Figure 2, the Ca XIV λ193.87 line ($\log(T_{\rm max}$ [K]) = 6.55), the core of the AR is similar to the XRT morphology (Figure 1, left).

We also selected two regions of coronal moss. These regions are indicated with boxes "M1" and "M2" in the Fe XII λ192.39 image. In the Fe XII image, we also show the areas selected for background subtraction. The intensities in these areas were averaged and later subtracted from the intensities averaged in the respective structures. We emphasize that the subtraction of coronal background is crucial for any diagnostics, as the background intensity can add up to several tens of percent of the intensity to the observed coronal structure (e.g., Del Zanna & Mason 2003). When choosing the backgrounds, we were trying to select areas which (a) contain as many pixels as possible in order to minimize the uncertainties of the observed intensities and (b) are spatially close to the respective structure.

Background for LC and M1 was selected in the upper left part of the EIS FOV (inclined box "BG1"), in a narrow dark region close to both LC and M1. The background BG2 for the moss M2 was chosen close by, in a region devoid of any emission in almost all of the spectral lines used in this work. Unfortunately, no background matching our criteria was found in the vicinity of LS. This is due to the fan loops spanning a large area. Although there is a relatively dark region located to the north of LS in Fe XII, cooler loops overlying the ARs can be seen in Fe IX, as well as hotter emission in Fe XV. For these reasons, we use the background BG1 for LS, as no other appropriate choice can be made.

In the remainder of this paper we will use background-subtracted intensities only. We will further refer to the structures whose intensities have been averaged and background intensities subtracted as "M1s," "M2s," "LCs," and "LSs."

2.3. Observations of the Quiet Sun

The observed off-limb QS area, together with a portion of the solar disk, is shown in Figure 3. Limb brightening is seen in cool lines such as Si VII λ257.37 and Fe IX λ188.5 ($\log(T_{\rm max}$ [K]) ≈ 5.8 for Maxwellian conditions). There is also a faint, arc-like, off-limb structure spanning the EIS FOV. It is most evident in Fe XIII λ202.04, and traces of it can also be

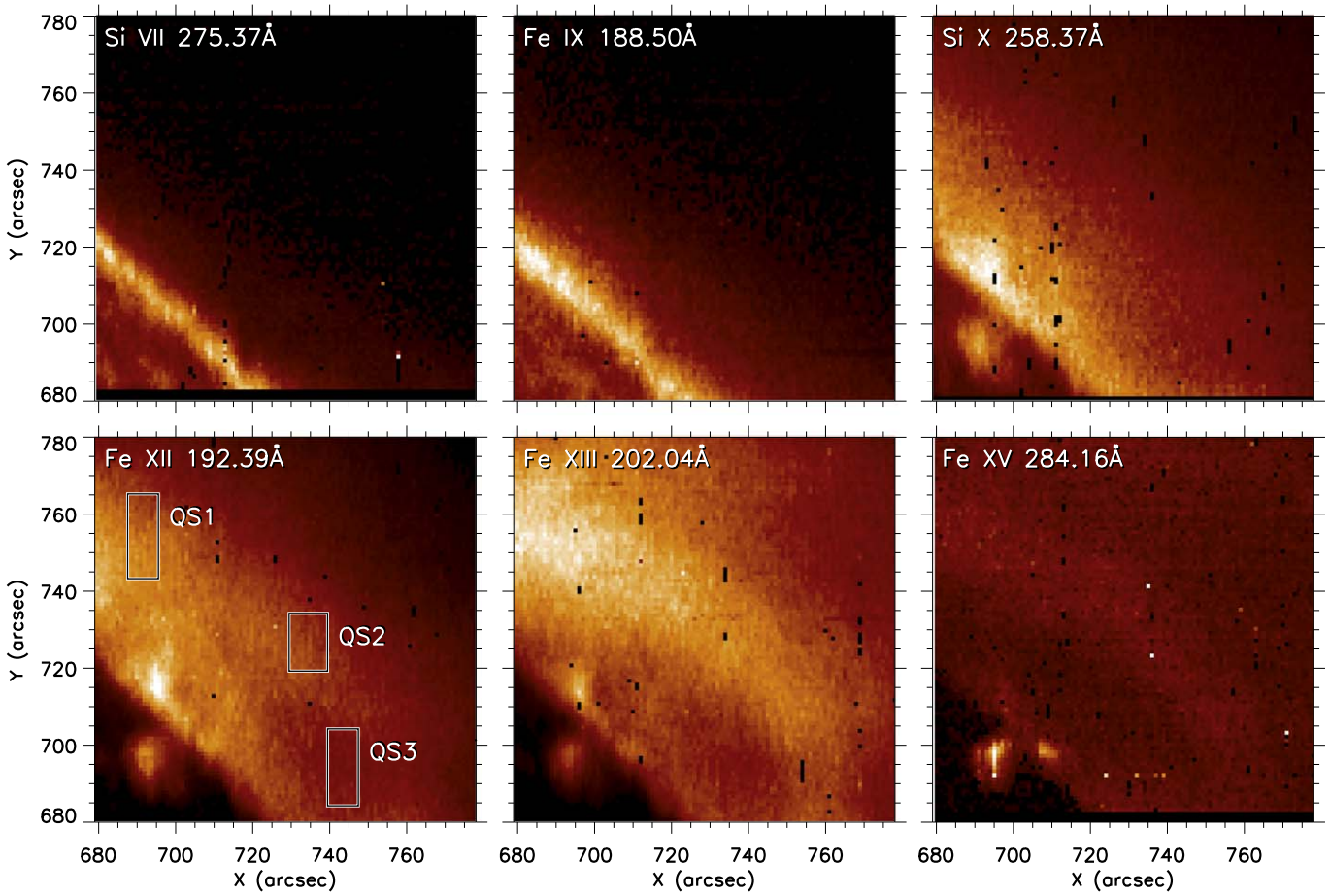

Figure 3. Context observations of the QS observed on 2007 March in different spectral lines observed by EIS. Boxes QS1–QS3 mark areas in which we averaged intensities that we used for later diagnostics of plasma.

seen in Fe XII and Fe XV. For purposes of plasma diagnostics, we selected three boxes QS1–QS3, which are shown in the bottom left panel of Figure 3. Since the QS contains diffuse emission, no background subtraction was performed. Note that there is also emission originating from the disk, in the form of a bright point present at coordinates of about [700″, 700″], seen in lines of ions with $\log(T_{\max}\ [\mathrm{K}]) \geqslant 6.15$.

Finally, we note that the same observation was used by Del Zanna (2012) when producing an atlas of coronal lines. Intensities averaged in an area that corresponds to our box QS1 can be found in Table A.1. therein.

3. Diagnostic Method

The properties of the observed optically thin coronal plasma are diagnosed using standard techniques based on comparisons of the observed line intensities with synthetic ones. Diagnostics of the electron density N_e (Section 3.2.1), temperature T, and the κ parameter (Section 3.2.3) are based on the line ratio technique, while the multithermal nature of the plasma is quantified using the differential emission measure (see Section 3.2.2).

The intensities of the spectral lines of diagnostic interest were obtained via line fitting, which included the subtraction of the neighboring continuum. Details of the fitting procedure are given in the Appendix, and the intensities of lines used in this work are listed in Table A1. The method for calculation of synthetic spectra is described in the following section.

3.1. Synthetic Spectra

3.1.1. Synthetic Line Intensities

The synthetic spectra are calculated here in the optically thin and coronal approximations. In optically thin conditions, the line intensity I_{ji} arising from a transition $j \rightarrow i$ between energy levels $j > i$ is given by the integral of the emissivity ε_{ji} along the line of sight l (see Mason & Monsignori Fossi 1994; Phillips et al. 2008):

$$I_{ji} = \int \varepsilon_{ji}(T, N_e, \kappa) dl = \int A_X G_{X,ji}(T, N_e, \kappa) N_e N_H dl, \quad (2)$$

where ε_{ji} is given by the product of the relative abundance A_X of the element X, the factor $N_e\ N_H \approx 0.83 N_e^2$, and the contribution function $G_{X,ji}$,

$$G_{X,ji}(T, N_e, \kappa) = \frac{hc}{\lambda_{ji}} \frac{A_{ji}}{N_e} \frac{N(X_j^{+k})}{N(X^{+k})} \frac{N(X^{+k})}{N(X)}. \quad (3)$$

There, λ_{ji} represents the wavelength of the emission line, hc/λ_{ji} is the photon energy, and A_{ji} is the Einstein coefficient for the spontaneous emission. The fractions $N(X_j^{+k})/N(X^{+k})$ and $N(X^{+k})/N(X)$ represent the fractions of the ion X^{+k} with the electron on the upper excited level j and the relative ion

abundance of the ion X^{+k}, respectively. In the coronal approximation, these fractions can be calculated separately, as the ionization and recombination processes occur dominantly from and to the ground level. This means that the ionization and recombination processes do not influence the relative level populations $N(X_j^{+k})/N(X^{+k})$ of the ion X^{+k}.

In the optically thin solar corona, the observed emission along the line of sight can originate at many different plasma temperatures. In such a case, Equation (2) for line intensity is customarily rewritten as

$$I_{ji} = \int A_X G_{X,ji}(T, N_e, \kappa) \mathrm{DEM}_\kappa(T) dT, \quad (4)$$

where the quantity $\mathrm{DEM}_\kappa(T) = N_e N_H dl/dT$ is the differential emission measure.

This definition assumes that there is a single-valued function, i.e., there is a particular distribution of plasma along the line of sight for which a DEM can be defined. We note that the assumption of optically thin plasma may not be valid everywhere in the solar corona. In particular, the well-known, bright Fe XII λ195.12 self-blend can be partially optically thick in AR conditions (Del Zanna et al. 2019). Throughout this work, we use the Fe XII λ192.39 line instead. This line originates from the same $3s^2\,3p^2\,3d\ ^4P$ system (see Table B.4 in Dudík et al. 2014), meaning that its intensity with respect to the λ195.12 self-blend is almost independent of plasma conditions, namely, N_e and κ.

3.1.2. Atomic Data

The atomic data used for spectral synthesis described in Section 3.1.1 are from the latest version 9 of the CHIANTI database (Dere et al. 1997, 2019). The ionization equilibrium for the non-Maxwellian κ-distributions is obtained using the method of Dzifčáková & Dudík (2013).

For the iron ions of importance for the diagnostics of κ in this work, we directly use the excitation cross sections from Del Zanna & Badnell (2014, Fe VIII), Del Zanna et al. (2014, Fe IX), Del Zanna et al. (2012a, Fe X), Del Zanna & Storey (2013, Fe XI, except levels 37, 39, and 41, for which the data of Del Zanna 2010 are used), Del Zanna et al. (2012b, Fe XII), Del Zanna & Storey (2012, Fe XIII), Liang et al. (2010) and Landi et al. (2012) for Fe XIV, Berrington et al. (2005, Fe XV), Liang et al. (2009, Fe XVI), and Liang & Badnell (2010, Fe XVII). These ions are the most important ones for the DEM diagnostics (Section 3.2.2). Finally, for the Si X, which is used for density diagnostics, we use the cross sections calculated by Liang et al. (2012). To obtain the corresponding excitation and de-excitation rates using these cross sections, the cross sections are integrated directly over the κ-distributions (Dudík et al. 2014).

3.2. Iterative Diagnostic Procedure

The line intensities are functions of three individual parameters, the electron density N_e, temperature T, and κ, the diagnostics of which is our objective. Of these, the T and κ are parameters of the distribution (Equation (1)) and must be diagnosed simultaneously. The line ratios sensitive to κ are also a function of electron density (Dzifčáková & Kulinová 2010; Mackovjak et al. 2013; Dudík et al. 2014, 2015, 2019; Dzifčáková et al. 2018). Therefore, the electron density N_e is diagnosed prior to diagnostics of T and κ. However, the theoretical curves for the diagnostics of N_e from density-sensitive line intensity ratios also depend slightly on T and κ (see, e.g., Figures 4–7 in Dudík et al. 2014). At the same time, for the diagnostics of T and κ, precise measurements of the electron density irrespective of T and κ are needed. In the work of Dudík et al. (2015), only constraints on the electron density were derived. To improve on this situation, we use a simple iterative-like approach, where the diagnosed quantities are refined in multiple steps.

In accordance with the approach of Mackovjak et al. (2013) and Dudík et al. (2015), we first obtain, in each structure, constraints on the electron densities, providing us with ranges of possible densities. This is done using the density-sensitive line intensity ratios, without any assumptions on the temperature structure of the emitting plasma, or the value of κ (see Dzifčáková & Kulinová 2010). Details on deriving these density ranges are provided in Section 3.2.1. These ranges can be large, up to 0.8 dex (e.g., Dudík et al. 2015), and can be narrowed only if the thermal structure of the emitting region is accounted for. We achieve this in conjunction with the $\mathrm{DEM}_\kappa(T)$ as follows. For the range of possible densities, a grid of $\mathrm{DEM}_\kappa(T)$ are reconstructed for all values of κ and N_e. Then, the density-sensitive ratio curves are weighted using the $\mathrm{DEM}_\kappa(T)$ obtained, thus removing the spread due to the unknown T. These DEM-weighted density-sensitive ratios are plotted for two extreme values of $\kappa = 2$ and a Maxwellian (Figure 5). This leads to an initial estimate on density, $N_{e,0}$.

The $N_{e,0}$ is dependent on κ only slightly, with the DEM-weighted ratios for $\kappa = 2$ yielding densities about 0.1–0.2 dex lower than the corresponding Maxwellian curves. This behavior of the density-sensitive coronal lines ratios with κ is well known (e.g., Dzifčáková & Kulinová 2010; Dudík et al. 2014, 2015; Dzifčáková et al. 2018) and occurs only for low $\kappa \to 2$ values. The resulting uncertainty in density is small enough to permit an initial estimate of the κ value using the ratio–ratio technique. Since the DEM-weighted density-sensitive ratios do not change appreciably for $\kappa \gtrsim 3$, we can restrict the initial estimate of κ to two extreme ranges, $\kappa \in (3, \infty)$ and $\kappa \lesssim 2$.

The next iteration consists of repeating the diagnostics of density. If the initial estimate yielded $\kappa \gtrsim 3$, the Maxwellian DEM-weighted density-sensitive ratios are used to obtain N_e. Conversely, if the initial estimate of κ yielded $\kappa \lesssim 2$, the DEM-weighted density-sensitive ratios for $\kappa = 2$ are used. The resulting densities are then used again to plot the ratio–ratio diagram and obtain the next iteration of κ.

In principle, this procedure could be repeated until converging values of N_e, $\mathrm{DEM}_\kappa(T)$, and κ are found. In practice, (i) the small differences of the DEM-weighted density-sensitive ratios for the Maxwellian and $\kappa = 2$, together with (ii) the insensitivity of DEM to N_e, (iii) calculation of the spectra for only the integer values of κ being used (Dzifčáková et al. 2015), and (iv) a rather large photon noise uncertainty of the measured ratios sensitive to κ, mean that two iterations, as described above, are sufficient for this diagnostics to converge.

3.2.1. Diagnostics of Electron Density

The electron density N_e is diagnosed by comparing the observed and theoretical ratios of line intensities. This method is well known and has been utilized in multiple studies, using ions of Fe (e.g., Watanabe et al. 2009; Young et al. 2009; Dudík et al. 2014, 2015; Mulay et al. 2017a; Polito et al. 2017), or other elements (e.g., Mackovjak et al. 2013; Mulay et al. 2017b). EIS observes numerous strong spectral lines that can be used for

measurements of density. Lines typically used are of Fe XI (Del Zanna 2010), Fe XII lines such as the λ186.89 and λ195.12 lines (Del Zanna 2012), or lines of Fe XIII, such as the λ196.53, λ202.04, or λ203.8 line (e.g., Young et al. 2007, 2009; Watanabe et al. 2009; Del Zanna 2011).

Because the densities measured from different ratios might differ (e.g., Dudík et al. 2015), here we combine results from four different line ratios of three different ions: Si X λ258.37/λ261.06, Fe XII λ186.89/λ192.39, Fe XIII λ196.53/λ202.04, and Fe XIII λ203.83/λ202.04. Note that the sensitivity of the Si X ratio is weak for $\log(N_e\,[\mathrm{cm}^{-3}]) > 9.5$. On the other hand, this ratio permits measurements of density below $\log(N_e\,[\mathrm{cm}^{-3}]) < 8$, which is important for constraining density in the QS. In the Fe XII ratio, we opted to use the λ186.89 line with the λ192.39 line instead of the λ195.12 one. The Fe XII λ186.89/λ192.39 ratio is sufficiently density sensitive in the range of $\log(N_e\,[\mathrm{cm}^{-3}]) \approx 7.5$–11.

Figure 4 shows the four density-sensitive ratios used. In this figure, the theoretical calculations are shown by black curves for the Maxwellian distribution, while the red curves stand for $\kappa = 2$. For each distribution, the ratios are shown at three different temperatures, corresponding to the temperatures of the peak of the ionization equilibrium, as well as where the ion abundance reaches 1% of the peak, which we take as extreme values (see Dzifčáková & Kulinová 2010; Dzifčáková & Dudík 2013). The span of the curves then describes the dependence of these ratios on both T and κ and is reduced in following steps of the iteration procedure by the DEM-weighting.

3.2.2. Differential Emission Measure

To fully address the temperature structure of the observed plasma, we examined the DEM and the emission measure distribution $\mathrm{EM}_\kappa(T)$, defined as

$$\mathrm{EM}(T) = \mathrm{DEM}_\kappa(T)\,\Delta T = \mathrm{DEM}_\kappa(T)\,\frac{T\Delta(\log T)}{\log e}. \qquad (5)$$

Here we employed the regularization inversion method of Hannah & Kontar (2012), used in conjunction with line intensities observed by EIS. The input parameters controlling the regularization were kept at their default setting. We varied the maximum χ^2 permissible to achieve robust solutions in as many temperature bins as possible, while attempting to recover smooth DEMs. In the AR structures the maximum χ^2 of the solutions was set to 3, while the value of 5 was needed for obtaining solutions in the QS. The uncertainties on the measured intensities included not only the photon noise but also the 20% calibration uncertainty of the instrument, which needs to be taken into account when lines from both the short- and the long-wavelength channels of the instrument are used.

The $\mathrm{DEM}_\kappa(T)$ are calculated as a function of κ, using $\kappa = 2$, 3, 5, 10, and Maxwellian. The corresponding temperature ranges were chosen to be $\log(T\,[\mathrm{K}]) = 5.6$–6.6 for QS and 5.7–6.8 for AR, with a step of 0.1. The lines of Fe VIII–Fe XVII are used for producing these DEMs. We note that relying on lines of a single element have the advantage of not introducing additional uncertainties due to elemental abundance variations. The temperature interval covered by these 10 Fe ions is also sufficient for quantifying the $\mathrm{DEM}_\kappa(T)$ not only at the temperatures of interest for diagnostics of κ but also to obtain sufficient constraints at both low and high temperatures for all κ values. Additional high-T constraints could in principle be obtained from other lines, such as from Ca XIV–Ca XVII, Ni XVII, or XRT observations, but these would require abundance analysis, which could be coupled to the diagnostics of κ, and as such are beyond the scope of this work.

An important assumption when analyzing DEMs is that the lines used for their construction are independent of density. This assumption is not always satisfied, as numerous lines of Fe XI–Fe XIII show at least weak sensitivity to density in the coronal conditions (see, e.g., Dudík et al. 2014). Therefore, we calculated the $\mathrm{DEM}_\kappa(T)$ as a function of the electron density in the range of $\log(N_e\,[\mathrm{cm}^{-3}]) = 8$–10 for all κ. Due to the choice of lines (see Appendix A.2), the sensitivity of the resulting DEMs to N_e is on the order of 10%, lower than uncertainty in the DEMs themselves. This let us use the obtained DEMs to refine the diagnostics of N_e (see Section 3.2.1).

3.2.3. Diagnostics of κ and T

To diagnose the κ parameter, we use the ratio–ratio method (Dzifčáková & Kulinová 2010; Dudík et al. 2014, 2015). The method consists of comparing two observed and theoretical line ratios. Typically, one ratio involves lines from two neighboring ions, which is dominantly sensitive to T. The second ratio is sensitive to κ owing to combining lines formed at different wavelengths. The sensitivity to κ arises from these lines having different excitation thresholds. In case of lines observed by EIS, one of the lines is usually observed in the short- and the other in the long-wavelength channel. The sets of theoretical ratios for different κ in the ratio–ratio diagram are plotted for a density (or range of densities) diagnosed a priori. Precise measurements of densities are advantageous, as the sets of curves for different densities overlap, which is a source of uncertainty in the resulting κ parameter (Dudík et al. 2014, 2015).

Here, we use the combinations of Fe XI and Fe XII lines also used by Dudík et al. (2015). The sensitivity to κ is produced by combination of the Fe XI λ182.17 and λ188.22 lines observed in the short-wavelength channel with the Fe XI λ257.55 and λ257.77 self-blends observed in the long-wavelength channel, identified for the first time in Del Zanna (2010) as a very useful diagnostic to measure T. The use of these lines is advantageous since the lines are well observed, as well as due to the relatively strong sensitivity to κ compared to other combinations of EIS lines. In Dudík et al. (2015), these Fe XI lines are coupled with the Fe XII lines such as the λ186.89 and λ195.12 lines in the conjugate ratio to provide strong temperature dependence.

A multitude of combinations of lines were used by Dudík et al. (2015). However, we opted not to use the Fe XI λ188.22 line for diagnostics of κ, because this line is blended with the Fe XII λ188.17 and Fe XI λ188.30 lines (see, e.g., Del Zanna 2012; Dudík et al. 2014), which are both density dependent, and we could not constrain amplitudes of Gaussians fitting these blends. Concerning the temperature-sensitive ratios, we again use the Fe XII λ192.39 line instead of the Fe XII λ195.12 line because of high χ^2 of its fit and possible optical thickness (Section 3.1.1).

Finally, note that the sets of ratio–ratio curves for diagnostics of κ are plotted as a function of T, assuming that the plasma is isothermal. In the case of multithermal plasma, these curves need to be weighted over the respective $\mathrm{DEM}_\kappa(T)$ (Dudík et al. 2015), producing a single predicted value for each ratio and κ (see Section 4.4).

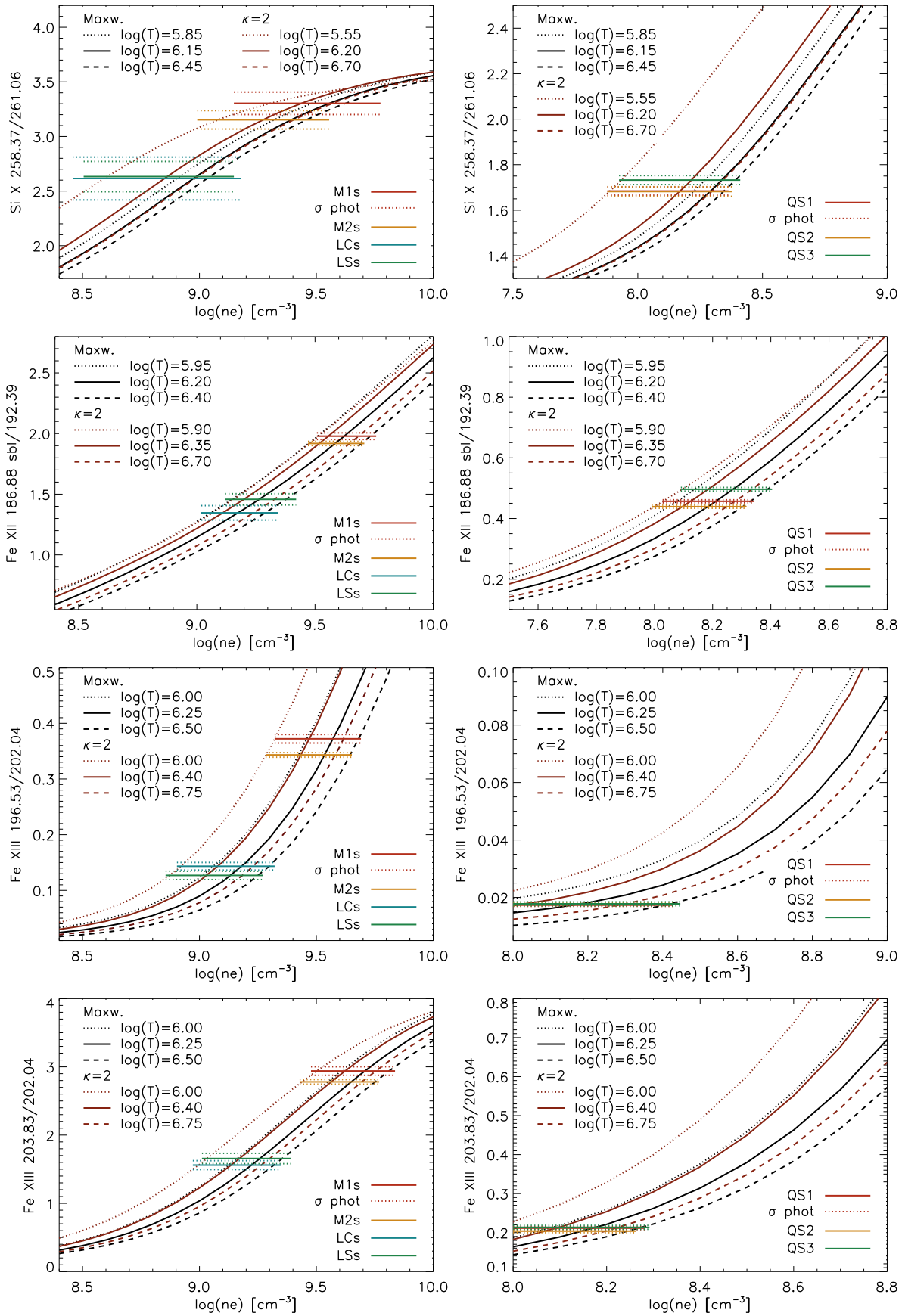

Figure 4. Diagnostics of density in selected boxes. Black and red curves are the theoretical ratios plotted for the Maxwellian and the $\kappa = 2$ distribution. Different line styles code different temperatures for which the ratios were calculated. Colored horizontal solid and dotted lines are the observed ratios and their respective $\sigma_{\rm phot}$ uncertainties.

Table 1
Initial Estimates on the Density Ranges Using the Line Ratio Technique

	QS1	QS2	QS3	M1s	M2s	LCs	LSs
Si X $\lambda258.37/\lambda261.06$	7.9–8.4	7.9–8.4	7.9–8.4	9.1–9.8	9.0–9.6	8.5–9.2	8.5–9.1
Fe XII $\lambda186.89/\lambda192.39$	8.0–8.3	8.0–8.3	8.1–8.4	9.5–9.8	9.5–9.7	9.0–9.3	9.1–9.4
Fe XIII $\lambda196.53/\lambda202.04$	8.0–8.4	8.0–8.4	8.0–8.4	9.3–9.7	9.3–9.7	8.9–9.3	8.9–9.3
Fe XIII $\lambda203.83/\lambda202.04$	8.0–8.3	8.0–8.3	8.0–8.3	9.5–9.8	9.4–9.8	9.0–9.4	9.0–9.4

4. Results

To determine the physical parameters of the emitting plasma in various observed structures in both the AR (Section 2.2.2) and the QS (Section 2.3), we use the iterative technique described in Section 3.2. Density ranges are obtained first, followed by $\mathrm{DEM}_\kappa(T)$ inversions, and then we perform the DEM-weighted density diagnostics and diagnostics of κ in two iterations.

4.1. Electron Densities

Density-sensitive line ratios as a function of the electron density N_e are shown in Figure 4. The theoretical ratios for the Maxwellian (black) and $\kappa = 2$ (red) are intersected by horizontal lines, which denote the observed ratios (solid) and their respective photon noise uncertainties σ_phot (dotted lines). The observed ratios intersect the theoretical ratios calculated using the Maxwellian (black curves). The left-hand side of Figure 4 shows the observed ratios in the AR, while the right-hand side shows the diagnostics in the QS.

As apparent from Figure 4, the natural spread of the theoretical ratios due to T and κ leads only to ranges of possible densities. These are summarized in Table 1. The lower limits on the density range for each structure and ratio were obtained from the intersection of the observed ratio minus its σ_phot uncertainty, with the theoretical ratio calculated assuming the $\kappa = 2$ distribution and the lowest temperature (dotted horizontal lines intersecting the dotted red curves in Figure 4). Conversely, the upper limit on the density range corresponds to the observed ratio plus σ_phot intersecting with the rightmost theoretical ratio, typically for the Maxwellian distribution and the highest temperature (dotted upper horizontal lines intersecting the black dashed curves). The initial density ranges can span about 0.3–0.9 dex in $\log(N_\mathrm{e}\,[\mathrm{cm}^{-3}])$ owing to the combination of the photon noise uncertainty and the dependence of density-sensitive ratios on T and κ. Note that since all density-sensitive ratios include lines observed at similar wavelengths in the same channel of EIS, the calibration uncertainty is not considered in density diagnostics.

As a next step in the iterative procedure, we used the $\mathrm{DEM}_\kappa(T)$ recovered in all of the observed structures to constrain the diagnostics of density. Examples of the DEM-weighted density-sensitive ratios are shown in Figure 5. This figure shows the Fe XII ratios, one panel for each of the structures investigated. In each panel, only two lines are shown, the black one for the Maxwellian distribution and the red one for $\kappa = 2$. The horizontal lines again stand for the observed ratios and their σ_phot uncertainties. For brevity we do not show the analogous panels for the other ratios. Instead, the initial estimates $N_{\mathrm{e},\,0}$ of the densities are summarized in Table 2. For each structure and line ratio, two densities are listed, one obtained for the Maxwellian and the other for $\kappa = 2$. These densities differ by about 0.1–0.2 dex, a value typical for density diagnostics for κ-distributions (Dzifčáková & Kulinová 2010; Mackovjak et al. 2013; Dudík et al. 2014, 2015; Dzifčáková et al. 2018). In all cases, the effect of the σ_phot uncertainties is at most 0.1 dex.

For QS1–QS3, M1s, and M2s, the densities diagnosed using all four ratios are consistent, with only minor differences. For LCs and LSs, we obtain consistent densities using the Fe XII and Fe XIII ratios. Si X indicates slightly lower densities, of up to 0.2–0.3 dex compared to the other ratios. The cause of this small inconsistency is unknown. Nevertheless, we include these results (see below) and note that excluding them would lead to higher densities and ultimately slightly stronger non-Maxwellian diagnostics (see Figure 7 and Section 4.3).

The initial estimate on DEM-weighted density, $N_{\mathrm{e}0}$, is also listed in Table 2. It was calculated as the average from the values listed and subsequently used to produce the first estimate on κ using the ratio–ratio technique (Section 4.3). Then, as described in Section 3.2, the final DEM-weighted density is obtained as the average of the density-sensitive DEM-weighted ratios using only Maxwellian or $\kappa = 2$ results, depending on the structure investigated.

The densities obtained are in good agreement with literature. For example, electron densities typically found in the QS are $\log(N_\mathrm{e}\,[\mathrm{cm}^{-3}]) = 8.2$ (e.g., Dere et al. 2007), while they are of the order of 9.0 in coronal loops (e.g., Tripathi et al. 2009; Young et al. 2009; Dudík et al. 2015) and 9.5 in the coronal moss (e.g., de Pontieu et al. 1999, 2009; Warren et al. 2008). Nevertheless, several comments on the density diagnostics, as well as the iterative method itself, are in order.

First, the uncertainties of the DEM-weighted densities are dominated by the photon noise and the spread of the results from different density-sensitive ratios and are ±0.1 dex at most. The uncertainties of the DEM-weighted theoretical ratios were evaluated by considering the DEMs with their respective errors and were found to be lower than the photon noise uncertainty; the DEM-weighted theoretical ratios do not differ from those in which we considered the uncertainties of DEMs by more than 1%.

Second, as already pointed out, the averaged DEM-weighted densities for the Maxwellian and $\kappa = 2$ do not differ for more than 0.2 dex (Table 2, Section 3.2). The effect of such small differences in densities on the ratios sensitive to κ does not exceed a few percent. Henceforth, averaging of the DEM-weighted densities into $N_{\mathrm{e},0}$ does not affect the first estimate on κ.

The differences between the initial estimates $N_{\mathrm{e},0}$ and N_e are 0.1 dex at most. Given the typical σ_phot uncertainties of ratios of line intensities (Figure 4), this indicates that single refinement of the density measurements via DEM and subsequently κ yields relatively precise results of density diagnostics, within 0.1 dex.

Finally, for AR, the resulting densities would be lower by about 0.2–0.3 dex if the background were not subtracted.

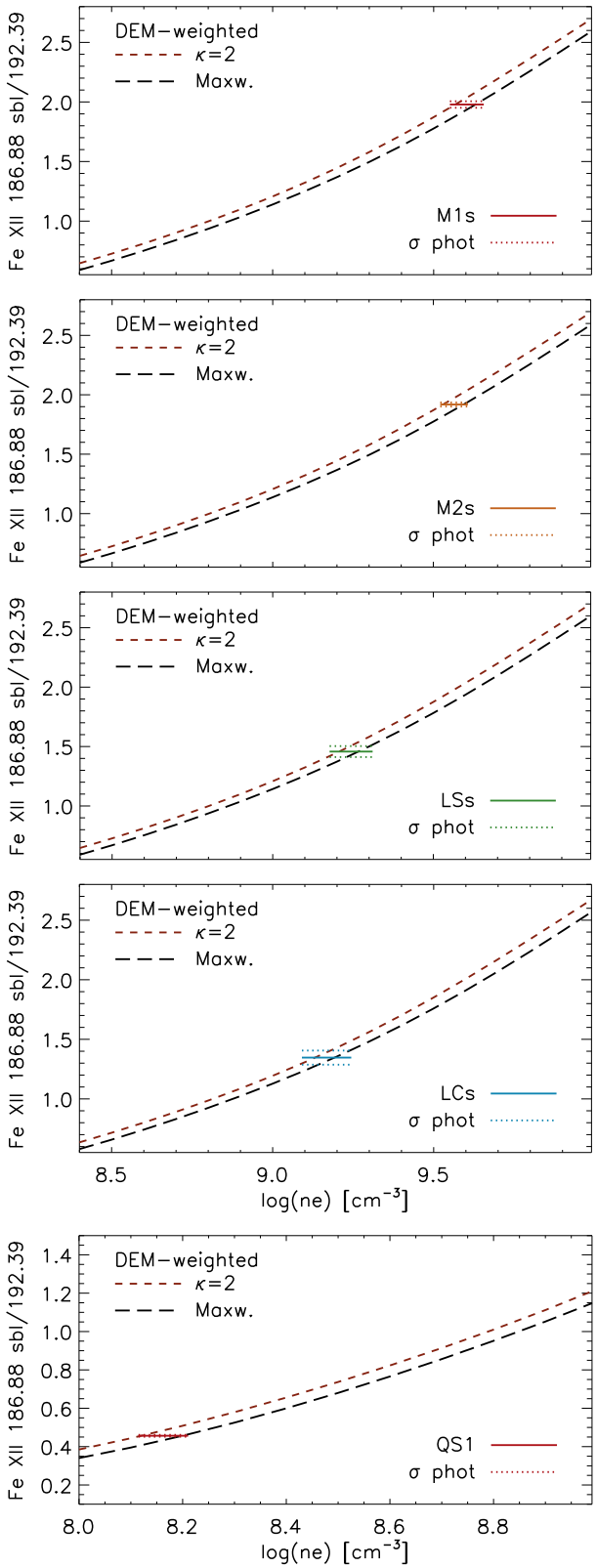

Figure 5. Effects of DEM on diagnostics of density. The black and red curves are DEM-weighted theoretical ratios plotted for the $\kappa = 2$ distribution (red short-dashed) and the Maxwellian distribution (black dashed). Horizontal colored solid and dotted lines are the ratios and their respective $\sigma_{\rm phot}$ uncertainties observed in different structures. Their color-coding is the same as in Figure 4.

4.2. Emission Measure Distribution in the Observed Structures

Recovered emission measure $\mathrm{EM}_\kappa(T)$ curves are shown in Figure 6. These are shown for the appropriate densities diagnosed (Table 2), although we note that in practice these curves are almost independent of N_e. The curves are plotted together with their respective errors in temperature (gray horizontal lines) and $\mathrm{EM}_\kappa(T)$ (gray vertical lines). Each $\mathrm{EM}_\kappa(T)$ panel is accompanied by the ratios $I_{\rm OBS}/I_{\rm DEM}$ of the observed to the DEM-predicted intensities. Due to similarities between DEMs of individual structures, we only show illustrative examples of results recovered for QS1, M2s, and LCs. The $\mathrm{EM}_\kappa(T)$ are shown for four different values of $\kappa = 2$, 3, 5, as well as the Maxwellian distribution.

4.2.1. Quiet Sun

In QS1, DEM for the Maxwellian distribution converged in a temperature range of $\log(T\,[\mathrm{K}]) = 5.7$–$6.4$. The corresponding $\mathrm{EM}(T)$ curve (top left panel in Figure 6) peaks at $\log(T\,[\mathrm{K}]) \approx 6.15$. For the κ-distributions, we found that the temperature at which the $\mathrm{DEM}_\kappa(T)$ curves peak shifts to higher temperatures, an effect that is well known (Mackovjak et al. 2014; Dudík et al. 2015). For the case of $\kappa = 2$, the $\mathrm{EM}_\kappa(T)$ curve peaks at $\log(T\,[\mathrm{K}]) \approx 6.35$, with the solution credibly converging in seven temperature bins only (bottom left panel of Figure 6). Many of the EM-loci curves plotted for different values of κ intersect in one point, indicating a possible near-isothermal nature of the QS plasma if κ-distributions are taken into account.

There are two reasons why the QS DEMs are only recovered in a narrow temperature range. First, signal observed in the QS boxes is typically lower than signal in the AR structures, which affects the credibility of DEMs (Hannah & Kontar 2012). Second, convergence of QS DEMs in a narrow temperature range is expected, as most of the strong lines observable there are formed in a narrow temperature range (Landi & Young 2010; Mackovjak et al. 2014). Indeed, almost isothermal DEMs peaking at about 1 MK are typical for the QS (see, e.g., Landi & Feldman 2003; Warren & Brooks 2009; Del Zanna 2012; Del Zanna & Mason 2018). Even though the temperature range in which we recovered DEMs in the QS boxes is narrow, it is sufficient enough for our purposes of predicting intensities of lines used in Section 4.4.

Finally, we note that the solutions in QS2 and QS3 are very similar to QS1.

4.2.2. Active Region

For the moss M2s, the $\mathrm{EM}(T)$ recovered for the Maxwellian distribution is broad and peaks at about $\log(T\,[\mathrm{K}]) = 6.25$ (Figure 6). At high temperatures, it is difficult to be constrained. The Fe XVII line at 254.9 Å is used for this purpose; however, this line is weak, which results in large uncertainties of its intensities. The DEM solutions converged with high confidence in the temperature range of $\log(T\,[\mathrm{K}]) = 5.7$–$6.7$. For the κ-distributions, a shift of the $\mathrm{EM}_\kappa(T)$ peaks to higher temperatures is again evident. For $\kappa = 2$, the $\mathrm{EM}_\kappa(T)$ peaks at $\log(T\,[\mathrm{K}]) \approx 6.45$ and then rapidly decreases for $\log(T\,[\mathrm{K}]) > 6.6$.

The $\mathrm{EM}_\kappa(T)$ curves for the loop LCs are shown in the right column of Figure 6. The maxima of $\mathrm{EM}_\kappa(T)$ are similar to those

Table 2
Density Diagnostics Using Selected Line Ratios with DEM-weighted Theoretical Ratios

	QS1		QS2		QS3		M1s		M2s		LCs		LSs	
Line Ratio	$\kappa = 2$	Mxw	$\kappa = 2$	Mxw	$\kappa = 2$	Mxw	$\kappa = 2$	Mxw	$\kappa = 2$	Mxw	$\kappa = 2$	Mxw	$\kappa = 2$	Mxw
Si X $\lambda258.37/\lambda261.06$	8.2	8.3	8.2	8.3	8.2	8.3	9.5	9.6	9.3	9.5	8.9	9.0	8.9	9.0
Fe XII $\lambda186.89/\lambda192.39$	8.1	8.2	8.1	8.2	8.2	8.3	9.6	9.7	9.5	9.6	9.1	9.2	9.2	9.3
Fe XIII $\lambda196.53/\lambda202.04$	8.0	8.1	8.0	8.2	8.0	8.1	9.5	9.6	9.4	9.6	9.1	9.2	9.0	9.2
Fe XIII $\lambda203.83/\lambda202.04$	8.1	8.2	8.0	8.1	8.1	8.2	9.6	9.7	9.6	9.7	9.1	9.3	9.2	9.3
$N_{e,0}$	8.2		8.1		8.2		9.6		9.5		9.1		9.1	
N_e	8.2		8.2		8.3		9.5		9.4		9.0		9.0	

Note. The typical uncertainties of these densities are <0.1 dex. The $N_{e,0}$ is the first estimate on DEM-weighted density, while N_e is the final density obtained from the iterative procedure.

for the moss M2s, but their shape differs for both high and low temperatures. First, the $EM_\kappa(T)$ curves for LCs contain a dip at the temperature roughly corresponding to the T_{max} of Fe IX, in agreement with this loop being faint at these temperatures. Second, with the low intensity of the Fe XVII $\lambda254.9$ line, it is still difficult to properly constrain the Maxwellian DEM at high temperatures using Fe lines only. The Maxwellian solution can, in some cases, even rise again at $\log(T\,[K]) \approx 6.7$. For this reason, in LSs (not shown), where the $\lambda254.9$ line was not observed at all, we exceptionally had to use the Ca XV $\lambda200.97$ line. Despite this, the recovered $EM_\kappa(T)$ are sufficient for predicting the line intensities (see the I_{OBS}/I_{DEM} ratios). In particular, note that the high- and low-temperature limits of the $EM_\kappa(T)$ do not play a role for recovering the intensities of Fe XI–Fe XII lines, which are critical for diagnostics of κ (see Section 4.4).

In summary, our EM $_\kappa(T)$ curves are broad, indicating that both M2s and LCs can be multithermal (see Fletcher & De Pontieu 1999; Tripathi et al. 2009, 2010; O'Dwyer et al. 2011; Dudík et al. 2015), at least if the Maxwellian distribution is considered. We note that the behavior of $EM_\kappa(T)$ with κ for M2s is similar to Mackovjak et al. (2014): the curves for low κ are similar, only shifted to higher temperatures. This is not true for LCs, where the low-T shoulder of the $EM_\kappa(T)$ becomes progressively less steep for low κ, as many of the EM-loci curves (Fe X–Fe XVII) nearly cross at the same point for $\kappa = 2$–3, possibly indicating plasma close to isothermality for such low values of κ.

4.3. Diagnostics of κ and T

The ratio–ratio diagrams for diagnostics of κ are shown in Figure 7. The dashed curves are the theoretical ratios, with colors denoting the values of κ. Black curves stand for the Maxwellian distribution, while the violet, green, orange, and red are for $\kappa = 10$, 5, 3, and 2, respectively. Pairs of ratio–ratio diagrams are shown. The left panels use the Fe XI $\lambda182.17/\lambda257.55$ ratio, while the right panels use the Fe XI $\lambda182.17/\lambda257.77$ ratio. On each panel, these curves are shown for the appropriate density N_e (Table 2, Section 3.2.1). For simplicity, we assumed that the densities between the individual areas of the QS, moss, and loops do not differ. This is justified, as these do not differ for more than 0.1 dex in log N_e. Black dashed curves intersecting different values of κ are the isotherms, with the corresponding temperatures shown in units of $\log(T\,[K])$.

The observed ratios for each structure are shown by crosses, whose size depends on the uncertainties. The thick inner crosses denote the photon noise uncertainties σ_{phot}. For completeness, the thin large crosses correspond to adding the 20% calibration uncertainty σ_{20}.

The diagnostic diagrams for the QS (top row of Figure 7) are shown for $\log(N_e\,[cm^{-3}]) = 8.2$. The observed ratios for QS1–QS3 are clustered near the Maxwellian curve, within one or several times the photon noise uncertainty. In the diagnostic diagram using the Fe XI $\lambda257.55$ line (left), the observed ratios either are located on the right-hand side of the theoretical ratios or intersect the theoretical ratios calculated for the Maxwellian distribution. The ratios involving the Fe XI $\lambda257.77$ line (right) are slightly shifted toward the left, still indicating either the Maxwellian or the $\kappa = 10$ distribution. The observed ratios also indicate temperatures $\log(T\,[K]) = 6.1$–6.2. These temperatures correspond well to the peak temperatures of DEMs recovered using the contribution functions calculated assuming the Maxwellian distribution.

The ratio–ratio diagrams for the LCs and LSs are shown in the middle row of Figure 7, plotted for the density of $\log(N_e\,[cm^{-3}]) = 9.0$. Both ratios indicate $\kappa \leqslant 2$ distribution, but the σ_{phot} uncertainties are large. The σ_{phot} uncertainties result in different constraints on κ from different ratios. These are summarized in Table 3, where we list the results of diagnostics from multiple line ratios, as indicated within the σ_{phot} uncertainty. Note that the diagram involving the Fe XI $\lambda257.77$ line (Figure 7, middle right) indicates strongly non-Maxwellian plasma with $\kappa \leqslant 2$, which is in accordance with results of Dudík et al. (2015).

The results obtained in the coronal moss boxes are similar. The ratio–ratio diagrams plotted for the density of $\log(N_e\,[cm^{-3}]) = 9.4$ are shown in the bottom row of Figure 7. Again, non-Maxwellian plasma is indicated, with $\kappa \lessapprox 3$ determined using the $\lambda257.55$ line, while the $\lambda257.77$ line suggests $\kappa \lessapprox 2$. Note that for M1s, the densities diagnosed were 9.5 (Table 2). For such densities, the theoretical ratios are shifted toward the right-hand side, leading to slightly higher departures from the Maxwellian distribution. Within the σ_{phot} uncertainty, the observed ratios typically intersect the isotherms corresponding to the temperatures of $\log(T\,[K]) = 6.2$, 6.3, or more (not shown). These again correspond to the peak temperatures of the $EM(T)$ curves of both LCs and M2s in DEMs obtained for the $\kappa = 3$, 5, and the Maxwellian distributions. Note that as the emission in the AR structures is distributed over a wide range of temperatures, this temperature diagnostic is indicative only and the effects of DEM will be discussed shortly.

In order to supplement our diagnostics of κ, we also constructed the ratio–ratio diagrams in which we used the Fe XII $\lambda186.89$ line instead of the Fe XII $\lambda192.39$ line. Since

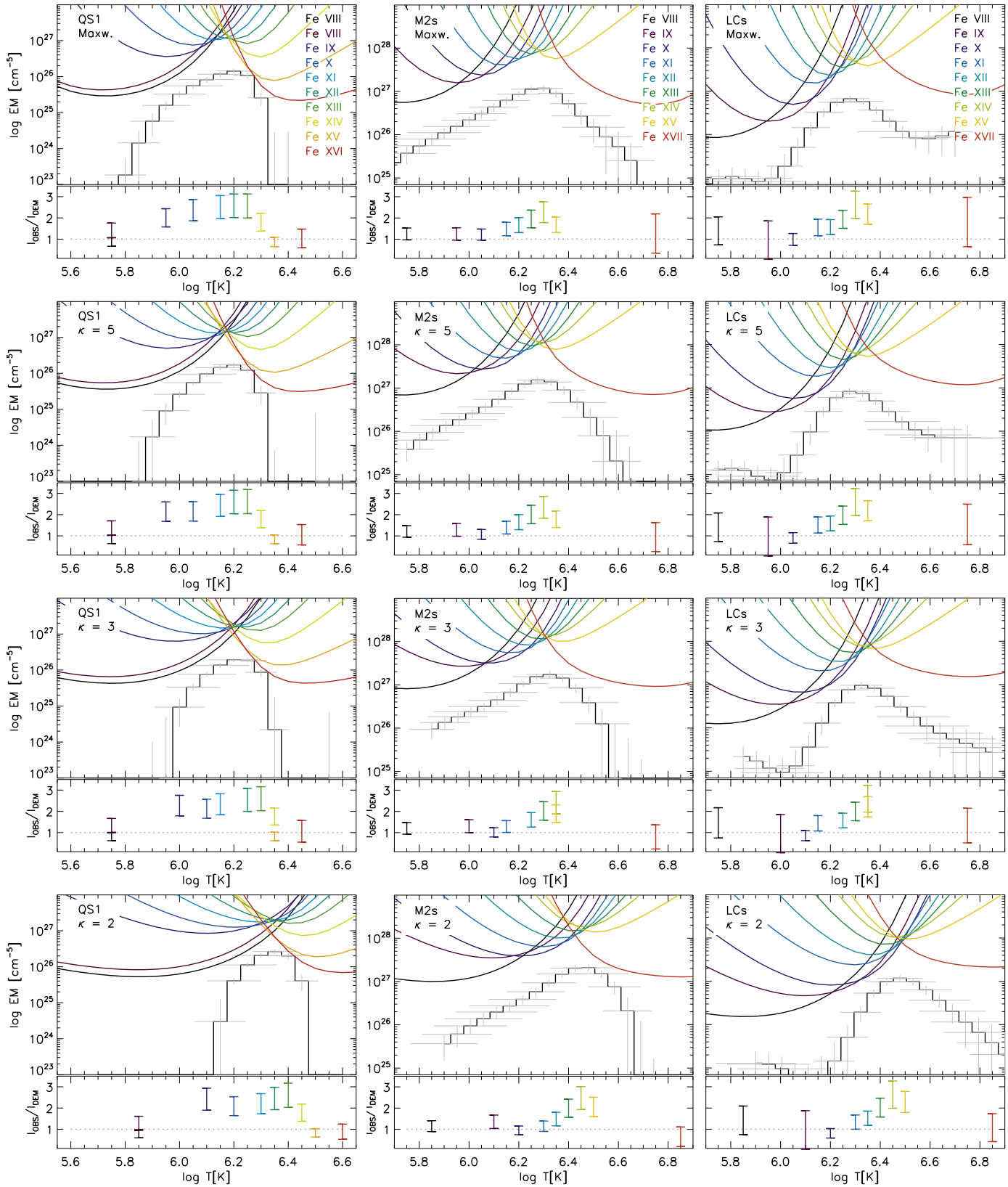

Figure 6. Emission measure distribution EM(T) for different values of κ. The EM-loci curves have been color-coded in order to distinguish between the different lines used. The left column shows the solutions recovered for QS1, the middle column shows the background-subtracted moss M2s, and the right column shows the solutions for the background-subtracted loop LCs. Below each solution, the ratios $I_{\rm OBS}/I_{\rm DEM}$ for each line used for construction of DEM are shown.

the ratio–ratio diagrams are comparable to those presented in Figure 7, we do not show them here. To supplement our diagnostics, we have, however, included them in Table 3.

Finally, as is apparent in Figure 7, the thin crosses, standing for the σ_{20} uncertainty, cross all of the theoretical ratios sensitive to κ, as well as multiple isotherms. Strictly speaking,

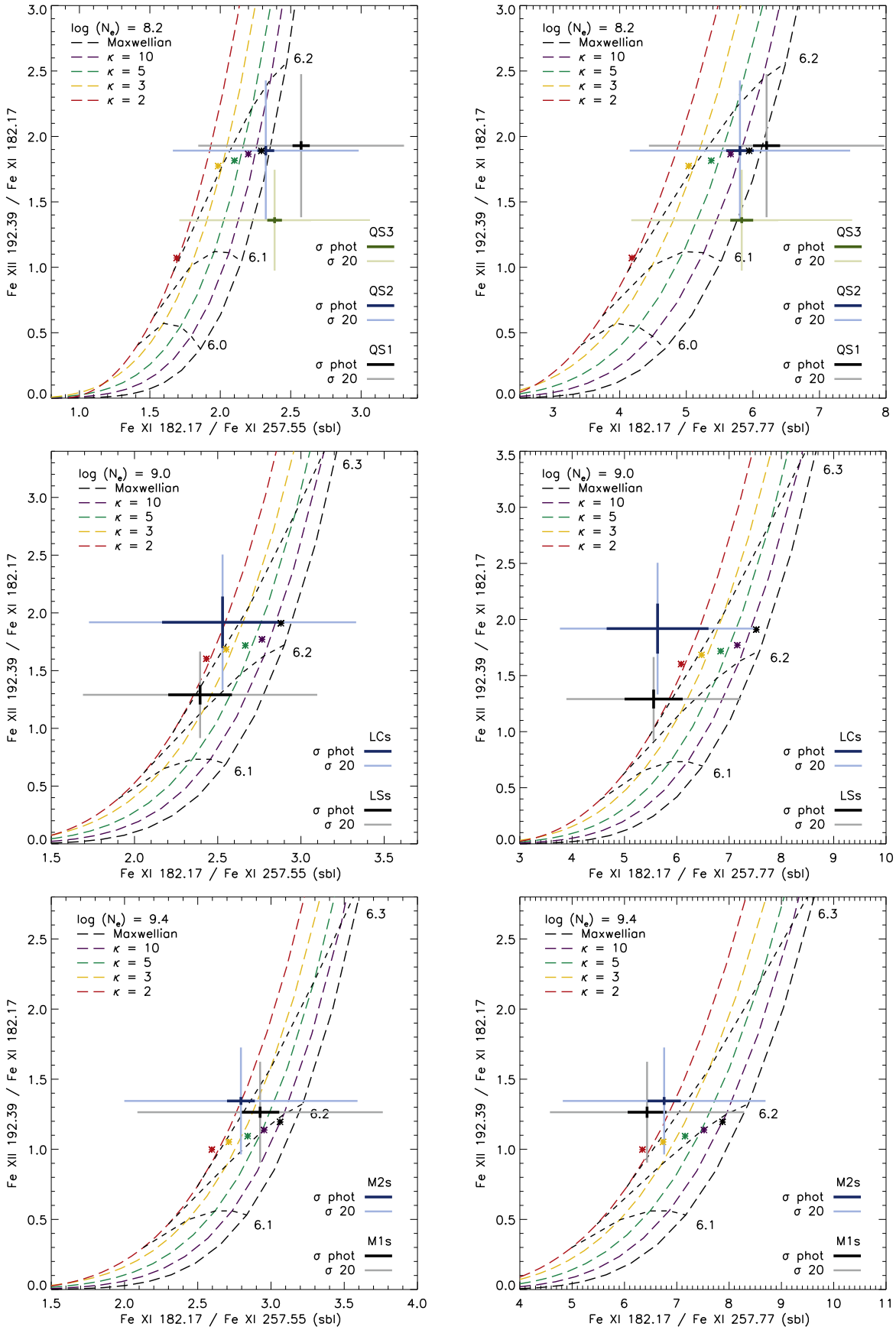

Figure 7. Ratio–ratio diagrams used for simultaneous diagnostics of κ and T plotted for densities measured a priori. Dashed colored lines are the theoretical ratios, which are intersected by the isotherms (black short-dashed lines). The blue, black, and green crosses represent the observed ratios with their $\sigma_{\rm phot}$ and σ_{20} uncertainties. Colored asterisks are the ratios predicted from DEMs produced for different κ.

Table 3
Results of Diagnostics of κ as Indicated by the Ratio–Ratio Diagrams within $\sigma_{\rm phot}$

Lines (Å)	QS	M1s	M2s	LCs	LSs
182.17, 257.55, 192.39	Maxwellian	$\kappa \leqslant 3$	$\kappa = 2$	$\kappa \leqslant 10$	$\kappa \leqslant 5$
182.17, 257.77, 192.39	$\kappa \geqslant 10$	$\kappa < 2$	$\kappa \leqslant 2$	$\kappa \leqslant 2$	$\kappa \leqslant 2$
182.17, 257.55, 186.89	Maxwellian	$\kappa \leqslant 3$	$\kappa \leqslant 2$	$\kappa \leqslant 5$	$\kappa \leqslant 3$
182.17, 257.77, 186.89	$\kappa \geqslant 10$	$\kappa < 2$	$\kappa < 2$	$\kappa < 2$	$\kappa < 2$

no constraints on κ can be obtained from error analysis alone. The only indication that the distribution in AR is different from that of the QS would then be that the measured Fe XI ratios are observed to be nearly the same in both the AR and QS. This result holds despite *an order-of-magnitude* difference in electron density. Therefore, if the distribution would be Maxwellian in both the AR and QS, the observed ratios should be different. We note, however, that the data we use here were acquired shortly after the start of the mission, indicating that the in-flight calibration and the associated calibration uncertainty should not play a large role in diagnostics.

4.4. Effects of $DEM_\kappa(T)$ on Diagnostics of κ

The ratio–ratio diagrams provide diagnostics of T and κ if analyzed plasma is isothermal. As we reported in Section 4.2, however, in many cases the observed plasma is multithermal, with the emission measures $EM_\kappa(T)$ shown in Figure 6. Therefore, we investigated the influence of the multithermality of plasma on the diagnostics of κ. To do that, we used the $EM_\kappa(T)$ obtained to predict the intensity ratios as a function of κ. These are shown as colored asterisks in each panel of the Figure 7 to facilitate comparisons with the observed ratios.

For the QS1, the predicted ratios converge on the observed one as the parameter κ increases. This conforms to the result that the QS is nearly Maxwellian, while the EM-predicted ratios for $\kappa = 2$ (red asterisks) are farthest from the observed ones.

In the case of LCs, the EM-predicted ratios confirm the results of diagnostics of κ. If the λ257.55 line is used, the observed ratios are closest to the EM-predicted ratios for $\kappa \leqslant 5$. Conversely, if the λ257.77 line is used, the closest match is found for $\kappa \leqslant 2$.

Contrary to these, the results obtained for M2s are ambiguous. For both the λ257.55 and the λ257.77 lines, none of the predicted ratios converge on the observed one. Moreover, in the ratio–ratio diagram involving the λ257.77 line, the observed ratio is far from the EM-predicted ones. The origin of this inconsistency is not known. Perhaps the electron distribution in the moss is not a κ-distribution. Alternatively, opacity effects due to unresolved chromospheric absorbing structures (de Pontieu et al. 2009) could explain this departure.

5. Discussion

5.1. Effects of the Background Subtraction on Diagnostics

Since the results of the diagnostics for the AR can be dependent on the choice of background, we investigated the effect of background subtraction on the results of diagnostics. As an example, we used the intensities observed in the loop LS but did not perform the background subtraction. Plasma diagnostics were performed again using the same iterative scheme (Section 3.2). The $DEM_\kappa(T)$ curves obtained with $\chi^2 = 3$ for all values of κ are smooth and have broad peaks.

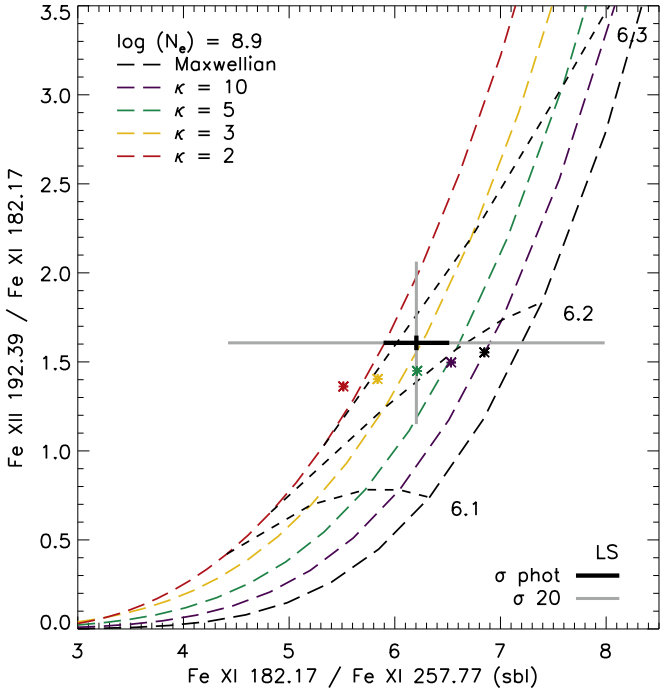

Figure 8. Ratio–ratio diagram used for simultaneous diagnostics of κ and T in the non-background-subtracted loop LS plotted for densities that were adopted using DEM-weighted theoretical ratios for the $\kappa = 2$ distribution. Dashed colored lines are the theoretical ratios, which are intersected by the isotherms (black short-dashed lines). The black cross represents the observed ratios with their $\sigma_{\rm phot}$ and σ_{20} uncertainties. Colored asterisks are the ratios predicted from DEMs produced for different κ.

The DEM-weighted electron densities obtained are $\log(N_{e,0}\ [\mathrm{cm}^{-3}]) \approx 9.0$ for the Maxwellian and 8.9 for the $\kappa = 2$ distribution. An initial estimate of κ using these densities led to finding non-Maxwellian plasma with $\kappa \approx 3$, which in turn led us to adopt the lower of the two densities diagnosed therein. An example ratio–ratio diagram involving the Fe XI λ257.77 line is shown in Figure 8. As the difference between the estimated and final measured densities is only 0.1 dex in $\log(N_{e,0}\ [\mathrm{cm}^{-3}])$, we still obtain $\kappa \approx 3$ in LS.

Recalling the results of diagnostics obtained using the background-subtracted intensities, we measured the density $\log(N_{e,0}\ [\mathrm{cm}^{-3}]) = 9.0$ and $\kappa \leqslant 2$. Note that the Fe XI ratio plotted on the X-axis, which is dominantly sensitive to κ, is 5.6 ± 0.6 for the background-subtracted (5.6 ± 0.6) case, while if the background is not subtracted, it is 6.2 ± 0.3. The difference between the measured values of κ is therefore due to a combination of the background subtraction and difference in the measured density, which both serve to decrease the value of κ and thus lead to the diagnosis of higher departures from the Maxwellian. This result shows the importance of the background subtraction.

5.2. Atomic Data Uncertainties

The atomic data are not in their state-of-the-art form, since they lack at least some of the high-energy levels. We now briefly summarize the effect of atomic data uncertainties on diagnostics of κ. A full discussion can be found in Dudík et al. (2015), who repeated the diagnostics of κ using older atomic data sets, corresponding to CHIANTI v7.1 (Dere et al. 1997; Landi et al. 2013), which have a lower number of energy levels compared to present version 9 of CHIANTI. These authors found that when these older atomic data are used, the curves in the ratio–ratio diagrams are shifted rightward, increasing the departure from the Maxwellian distribution. Furthermore, the older atomic data would lead to difficulties in density diagnostics, with the Fe XII density-sensitive ratio indicating inconsistent densities with respect to Fe XIII, typically higher by about 0.5 dex (see Del Zanna et al. 2012b, for further details).

The present atomic data, corresponding to CHIANTI v9, still lack $n \geqslant 5$ energy levels. As discussed by Dudík et al. (2015), however, including these higher energy levels and the cascading from them is unlikely to change the results of diagnostics, as the synthetic line intensities would not increase by more than about 10%, with details depending on the line.

5.3. Interpretation of the Results

The result that the QS is Maxwellian with nearly the same temperatures as seen with previous instruments (e.g., Landi & Feldman 2003) is an important one, because it indicates that both our iterative diagnostic procedure and the latest atomic data work well. Moreover, since we used data observed shortly after the start of the Hinode mission, the degradation of the instrument could have been neglected.

The fact that the QS is consistently Maxwellian regardless of location, while the AR structures tend to be non-Maxwellian, can have implications for the mechanism heating the corona. Since the AR spectra show departures from the Maxwellian, even after accounting for multithermal plasma, this could indicate that the coronal heating mechanism operating there accelerates particles more efficiently than in the QS. Presumably, the heating frequency in ARs is higher than in the QS and sufficient for the plasma to remain energized and non-Maxwellian. In both these cases, the non-Maxwellian effects need to be taken into account in modeling the coronal heating and coronal loop evolution, since at $\kappa = 2$ about 80% of the kinetic energy of particles is carried by the high-energy tail (Oka et al. 2013). In addition, for $\kappa = 2$, the coronal ions are formed at higher temperatures than for the Maxwellian (Dzifčáková & Dudík 2013), which also has consequences for loop energetics.

An alternative explanation for both the non-Maxwellianity and the multithermality of plasma is that the plasma is out of the ionization equilibrium. Such a situation can arise, for example, as a result of effects of a periodic electron beam as investigated by Dzifčáková et al. (2016). To an initially undisturbed bulk of coronal plasma, high-energetic electrons in the periodic beam are injected. This drives the plasma out of the ionization equilibrium at all times, irrespectively of the frequency of the beam. As the plasma is out of equilibrium, it appears multithermal, and since there are energetic electrons, the spectra are also non-Maxwellian. The degree of these effects is manifested in the shapes of DEMs, which authors recovered using the same method and ions as we did here, but with synthesized line intensities. DEMs presented in the bottom two rows of Figures 6 and 7 therein are very similar to those we obtained in the structures selected in the AR (Figure 6, middle and right columns).

Finally, an additional effect might contribute to the observed difference in terms of κ between the QS and AR. The total cooling time $\tau_{\rm cool}$ is inversely proportional to the plasma pressure as $\tau_{\rm cool} \sim P^{-1/6}$ (Equation (A2) in Cargill 2014). Since $P \simeq N_{\rm e}T$, given the low densities observed in the QS, this implies that the cooling time of the QS plasma should be longer compared to the ARs. As a consequence, if the frequencies of heating events in ARs and the QS were the same, the QS plasma would also be observed as non-Maxwellian, which does not conform to our observations. Note that this comparison is only speculative, since the AR appears to be hotter than the QS, at least judging by the peaks of the $\mathrm{DEM}_{\kappa}(T)$—an effect more pronounced if the $\kappa = 2$ in the AR spectra is considered compared to the Maxwellian QS (Figure 6).

6. Summary

In this manuscript we present diagnostics of the non-Maxwellian κ-distributions in an AR and QS observed by Hinode/EIS. Our results indicate that the plasma in the QS is Maxwellian, while AR loops and moss show strong departures from the Maxwellian distribution with $\kappa \lessapprox 3$.

The method we used for diagnostics of κ involves emission lines observed in both wavelength channels of the EIS instrument. To avoid problems with the decay of sensitivity and changes in the in-flight calibration, we used spectral atlases taken near in time and soon after the start of the mission. We chose three QS areas QS1–QS3 for analysis, along with two coronal moss areas M1s and M2s, as well as closed loop LCs and fan loop LSs. From the intensities observed in the moss and loops, we subtracted their respective backgrounds.

Since the diagnostics of κ is contingent on the diagnostics of electron density, the density had to be diagnosed first. However, the density-sensitive ratios of coronal lines are themselves dependent on both temperature and κ. In addition, the observed structures can be multithermal, with the $\mathrm{DEM}_{\kappa}(T)$ being dependent on κ. Therefore, we developed a simple iterative procedure that progressively constrains the parameters to be diagnosed—electron density, $\mathrm{DEM}_{\kappa}(T)$, and finally the non-Maxwellian parameter κ. Since the DEMs are largely insensitive to density and the density diagnostics is not strongly dependent on κ, the iterative procedure converges in two iterations.

In addition to being Maxwellian, the QS is also nearly isothermal, with $\mathrm{EM}(T)$ peaking at $\log(T\,[\mathrm{K}]) \approx 6.2$. The densities there were found to be $\log(N_{\rm e}\,[\mathrm{cm}^{-3}]) = 8.2$–$8.3$.

In AR, both LCs and LSs were found to be strongly non-Maxwellian, and both have densities of about 9.0. The corresponding $\mathrm{EM}_{\kappa=2}$ peaks at $\log(T\,[\mathrm{K}]) = 6.3$, with a strong increase at lower temperatures and a more gradual drop at higher temperatures. The EM-loci plot for $\kappa = 2$ is also closer to isothermal than the corresponding Maxwellian one. In the moss, we find densities of about 9.4–9.5. The $\mathrm{EM}_{\kappa}(T)$ curves are again steeper for lower κ than for Maxwellian, with the EM-loci curve for $\kappa = 3$ indicating a near-isothermal plasma for Fe X–Fe XVII. Although the moss appears to be

strongly non-Maxwellian, after accounting for multithermal effects, our results are not conclusive, as the DEM-predicted ratios are far from the observed ones. This could indicate either that the moss cannot be described by a κ-distribution or the presence of unresolved, low-lying absorbing structures.

Our results that the QS is Maxwellian could be taken as an indication that the atomic data, the ground calibration of the instrument, and the iterative diagnostic procedure work well. Furthermore, these results strengthen the presumption that the AR loops can be strongly non-Maxwellian, all the more so since the Fe XI ratios used for diagnostics of κ are observed to be nearly the same in the QS and the AR, independently of the electron density. In particular, the Fe XI λ182.17/λ257.55 ratio is observed to be about 2.5, while the Fe XI λ182.17/λ257.77 ratio is about 6.0 in both QS and AR loops. Even though we performed averaging of intensities over many pixels in structures selected within both observations, and the signal-to-noise ratio of the relatively weak Fe XI λ257.55 and λ257.77 lines is high, the diagnostics of κ presented here is severely limited by the 20% calibration uncertainty of the instrument, which leads to the observed ratios having larger uncertainties than the spread of the ratio–ratio curves for diagnostics of κ. Nevertheless, since both the QS and the AR were observed close in time, we are convinced that our results are not influenced by the calibration issues (and their uncertainties).

This work was supported by the Charles University, project GA UK 1130218. J.L., J.D., and E.D. acknowledge support from grant No. 18-09072S of the Grant Agency of the Czech Republic, as well as institutional support RVO:67985815 from the Czech Academy of Sciences. J.D., J.L., G.D.Z., and H.E.M. acknowledge support from STFC (UK) and the Royal Society via the Newton Fellowships Alumni Programme. Hinode is a Japanese mission developed and launched by ISAS/JAXA, collaborating with NAOJ as a domestic partner and NASA and STFC (UK) as international partners. Scientific operation of the Hinode mission is conducted by the Hinode science team organized at ISAS/JAXA. This team mainly consists of scientists from institutes in the partner countries. Support for the post-launch operation is provided by JAXA and NAOJ (Japan), STFC (U.K.), NASA (U.S.A.), ESA, and NSC (Norway).

Appendix
Line Fitting and Intensities

The intensities of the observed spectral lines used for diagnostic purposes were obtained via fitting of the observed spectra with Gaussian fits. The line profiles were averaged in the structures selected in Sections 2.2.2 and 2.3. We fitted the spectra manually using the fitting routine `xcfit` to be able to control and constrain not only the parameters of fits of line blends, such as the number of Gaussians, their widths, positions, and maxima of amplitudes, but also the level of the continuum. Fitted intensities of spectral lines further used in this work are listed in Table A1. We fitted the averaged line profiles within each of the box of interest including coronal background. Background subtraction was performed by subtracting the fitted background intensities.

A.1. Lines Used for Diagnostics of N_e *and* κ

A.1.1. Si X

In coronal conditions, the Si X λ258.37 and λ261.06 lines are neither blended nor self-blended. The λ258.37 line was fitted using a single Gaussian with reduced chi-squared (hereafter $\chi^2_{\rm red}$) of $\approx$4. A major contribution to the residuals originated in wings of the line, which were not well fitted by the Gaussian. We attempted to improve this fit by adding an additional low and broad Gaussian to fit the wings separately. The highest difference between the intensities obtained using one- and two-Gaussian fits was about 4%, which is a factor of 5 lower than the calibration uncertainty of the instrument. We note that we were unable to fit the wings of some of the other lines whose fitting is described in the following sections. As the fitting of their wings using additional Gaussian led to similar results as in the case of the Si X λ258.37 line, for simplicity we used single-Gaussian fits only, where applicable. In spectra averaged in the AR structures we also found an unknown weak line with centroid at $\approx$258.2 Å, which was fitted using one Gaussian. The weaker λ261.06 line was fitted using a single Gaussian with $\chi^2_{\rm red}$ of the fit $\approx$2.

A.1.2. Fe XI

The Fe XI λ182.17, λ257.55, and λ257.77 lines were used in this work for diagnostics of κ. The λ182.17 line is not blended and was fitted with a single Gaussian. In the long-wavelength channel of EIS, both the λ257.55 and λ257.77 lines are located close to one another in the neighborhood of multiple spectral lines, such as Si X λ257.2, Fe X doublet at 256.26 Å, Fe XIV λ257.4, and Fe XI λ257.9. Both lines were therefore fitted within one spectral window, broad enough to apply multiple single-Gaussian fits of the neighboring lines and constrain the value of the continuum. Single-Gaussian fits were also sufficient for the Fe XI λ257.55 line, which is self-blended with three additional transitions at 257.54, 257.55, and 257.56 Å (Dudík et al. 2014), i.e., below EIS wavelength resolution. Single-Gaussian fits were also applied for the λ257.77 line. The weak self-blend at 257.73 was not discerned in the spectra.

A.1.3. Fe XII

The strong lines of Fe XII are found close to the peak of the effective area of the short-wavelength channel of EIS (see, e.g., Del Zanna 2013b) and are commonly used for diagnostics of density. The λ186.89 line consists of three self-blending transitions at 186.86, 186.89, and 186.93 Å. The line is also blended in both wings with the Si XI λ186.84 line (Young et al. 2009) and with an unknown line at $\approx$186.98 Å. The latter resulted in a pronounced red wing in all of the investigated areas and required fitting with an additional Gaussian. The strong λ195.12 line is self-blended with the λ195.18 line, whose intensity is $<$10% of the stronger line for $\log(N_{\rm e}\ [{\rm cm}^{-3}]) < 10$ (Young et al. 2009). Unfortunately, even in structures in which this blend was taken into account, we were not able to fit this line with $\chi^2_{\rm red}$ lower than 20, reaching up to $\approx$100 in some cases. Again, a significant contribution to the residuals originated in wings of the line, for which the Gaussian fit is not adequate. The situation has repeated itself in the case of another strong Fe XII λ193.51 line. We finally opted to use the λ192.39 line, which is neither blended nor self-blended, and

Table A1
Intensities of Emission Lines Observed in the Analyzed Structures

Line		log (T_{max} [K])		Structure						
λ (Å)	Ion	Maxw.	$\kappa = 2$	M1s	M2s	LCs	LSs	QS1	QS2	QS3
182.17	Fe XI	6.15	6.30	1480 ± 44	1271 ± 30	412 ± 47	788 ± 49	227 ± 4	208 ± 4	259 ± 4
184.54	Fe X	6.05	6.15	1262 ± 30	974 ± 21	211 ± 32	829 ± 37	338 ± 3	327 ± 4	518 ± 4
185.21	Fe VIII	5.65	5.60	528 ± 28	512 ± 17	79 ± 30	295 ± 35	27 ± 1	25 ± 1	68 ± 2
186.89	Fe XII	6.20	6.35	3703 ± 36	3278 ± 24	1064 ± 39	1482 ± 37	200 ± 2	173 ± 2	175 ± 2
192.39	Fe XII	6.20	6.35	1872 ± 18	1709 ± 12	790 ± 20	1017 ± 19	438 ± 2	393 ± 2	352 ± 2
194.66	Fe VIII	5.65	5.60	92 ± 12	102 ± 4	unobs.	88 ± 13	9 ± 1	8 ± 1	18 ± 1
196.53	Fe XIII	6.25	6.40	1059 ± 11	929 ± 7	298 ± 12	217 ± 11	17 ± 0.4	15 ± 0.4	12 ± 0.5
197.86	Fe IX	5.90	6.00	155 ± 16	129 ± 15	19 ± 17	156 ± 15	37 ± 1	35 ± 1	76 ± 1
202.04	Fe XIII	6.25	6.40	2847 ± 50	2706 ± 31	2078 ± 53	1710 ± 51	1001 ± 4	860 ± 4	670 ± 3
203.83	Fe XIII	6.25	6.40	8367 ± 102	7523 ± 63	3241 ± 107	2833 ± 98	212 ± 4	175 ± 3	143 ± 3
211.32	Fe XIV	6.30	6.45	5813 ± 354	5642 ± 178	3693 ± 407	2308 ± 332	294 ± 7	248 ± 8	174 ± 8
249.17	Ni XVII	6.50	6.70	446 ± 31	287 ± 25	742 ± 34	unobs.	unobs.	unobs.	unobs.
254.90	Fe XVII	6.60	6.65	13 ± 13	3 ± 3	5 ± 3	unobs.	unobs.	unobs.	unobs.
257.55	Fe XI	6.15	6.30	506 ± 17	455 ± 16	163 ± 14	329 ± 17	88 ± 1	89 ± 2	108 ± 2
257.77	Fe XI	6.15	6.30	230 ± 11	188 ± 10	73 ± 10	142 ± 11	37 ± 1	36 ± 1	44 ± 1
258.37	Si X	6.15	6.15	1975 ± 29	1602 ± 27	601 ± 24	972 ± 27	318 ± 2	288 ± 2	330 ± 2
261.06	Si X	6.15	6.15	598 ± 16	508 ± 15	230 ± 15	369 ± 17	189 ± 2	171 ± 2	190 ± 2
262.98	Fe XVI	6.45	6.60	768 ± 19	695 ± 19	1036 ± 20	130 ± 18	2 ± 1	1 ± 4	1 ± 0.5
275.37	Si VII	6.15	6.15	126 ± 11	186 ± 9	unobs.	230 ± 12	15 ± 1	14 ± 2	44 ± 1
284.16	Fe XV	6.35	6.50	9496 ± 93	11616 ± 103	8054 ± 93	3767 ± 95	164 ± 2	140 ± 2	113 ± 2

we managed to fit it with $\chi^2_{red} = 2$–17, depending on the analyzed structure.

A.1.4. Fe XIII

We used the well-known lines at 196.53, 202.04, and 203.83 Å. The λ196.53 line was in both the AR and QS found to be weaker than its self-blended companion, the Fe XII λ196.6 line. However, the lines are well separated and can each easily be fitted with a single Gaussian. In all of the analyzed structures, we obtained fits of this spectral window with χ^2_{red} close to 1. The λ202.04 line is self-blended with the λ202.0 line but can be fitted using a single Gaussian. χ^2_{red}s of its fits were relatively high, reaching up to ≈20 based on the analyzed structure. High residuals were again found in the wings of the line. The λ203.83 line is a complex self-blend composed of five transitions at 203.77, 203.8, 203.81, 203.83, and 203.84 Å (Young et al. 2009). Moreover, the blue wing of the line is blended by the Fe XII λ203.73 line, whose intensity reaches 15%–20% of its stronger companion. Two Gaussians were needed to fit this multiplet, and χ^2_{red} of the recovered fits were found to be around 15 for the coronal moss and close to 1 in the QS, loops, and background.

A.2. Lines Used in DEM Analysis

A.2.1. Low-T Range

Both in the QS and the AR structures, the DEMs were at $\log(T\,[\mathrm{K}]) \approx 5.75$ constrained using Fe VIII λ185.21 and λ194.66 lines. The λ185.21 line is blended by the Ni XVI λ185.23 line, whose intensity in synthetic spectra reaches up to 18% intensity of the λ185.21 line. As this contribution is within the calibration uncertainty of EIS, we did not remove it. The weaker λ194.66 line is weakly blended with the Fe XII λ194.61 line. This line is also close to the Ni XII λ194.82 and Fe XII λ194.90 lines, which are within the blue wing of the strong Fe XII λ195.12 line. After adding a Gaussian to all the lines in this spectral window, we obtained good fits with $\chi^2_{red} \rightarrow 2$ in some cases. In both loops LS and LC, where the Fe VIII lines were weak, the fitting resulted in high σ_{phot} uncertainties comparable to the 20% calibration uncertainty of EIS. Concerning the weak blends of both Fe VIII lines, note that the positions of the minima of their EM-loci curves (see Q1 DEMs in Figure 6) are similar. Therefore, even though we did not exclude the contributions of the blending lines, both lines served equally good as the lower-temperature constraints of DEMs. At temperatures of $\log(T\,[\mathrm{K}]) \approx 6.0$ we used the Fe IX λ197.86 and Fe X λ184.54 lines. In the AR spectra, the Fe IX λ197.86 line was found to be surrounded by multiple weaker lines, such as Fe VIII λ197.36, Fe XIII λ197.43, and Ni XI λ198.39, all of which required adding an additional Gaussian. We also found a weak unknown blend at ≈197.7 Å. Despite the complexity of the fit of the Fe IX λ197.86 line, we obtained $\chi^2_{red} < 10$ in all areas within the AR. In the QS spectra, this line was only accompanied with an unknown weak line at ≈198.09 Å. The Fe X λ184.54 line in the ARs is blended with the Ar XI λ185.52 line, but the contribution of this blend reaches only about 1% for $\log(N_e\,[\mathrm{cm}^{-3}]) \approx 9.5$ and vanishes for lower densities. This line was in all AR structures fitted using a single Gaussian with $\chi^2_{red} \approx 1$. The χ^2_{red} was higher in the QS (≈10) owing to high residuals in the red wing of the line, due to an unknown blend.

We note that for constraining DEMs in this range of temperatures, the Si VII λ257.37 line can also be used. The line is not blended and can be fitted with $\chi^2_{red} \approx 1$ without problems. However, to avoid possible inconsistencies linked to element abundances, we in all structures but the background-subtracted loop LS used lines of iron ions only.

A.2.2. Mid-T Range

Constraints for $\mathrm{DEM}_\kappa(T)$ near their peaks were obtained by using the Fe XI λ182.17, Fe XII λ192.39, and Fe XIII λ202.04 lines, whose fitting was already described. At higher temperatures near the peak, EIS observes multiple strong lines of Fe XIV, most of which are either density sensitive or blended (e.g., Del Zanna 2013a). In accordance with Del Zanna (2013b), we used

the λ211.32 line, which we found to be the least sensitive to density. We note that in the QS spectra we observed this line to be accompanied by the Ni XI λ211.43 line, which we fitted with a single Gaussian. Fitting of the Fe XV λ284.16 line in AR resulted in obtaining high $\chi^2_{\rm red}$, reaching up to $\approx$100 in M1. Just as in the case of the Si X λ258.37 or Fe XII λ195.12 lines, the Gaussian curve is likely not suitable for reproducing the wings of the line. This line is known to be blended with the Al IX λ284.03 line, but based on the symmetry of the residuals observed in wings of this line, this blend was either weak or not present at all in AR spectra. On the other hand, in the QS, the intensity of this blend was found to reach $\approx$30% of the intensity of the λ284.16 line. We note that this observation is not consistent with the synthetic spectra, because the spectral synthesis performed with Maxwellian QS and AR DEMs suggests a much lower contribution of this blend, about 1%–2% only.

A.2.3. High-T Range

In the QS at $\log(T\,[\mathrm{K}]) > 6.3$ we observed only very little emission. The Fe XVI λ262.98 line, which we used for constraining the DEMs at corresponding temperatures, was very weak, reaching typically only about 1–2 erg cm^{-2} s^{-1} sr^{-1} in fits with $\chi^2_{\rm red} = 1$–11. In the QS, around 15% of the intensity of this line is due to the Fe XIII λ262.99 blend, whose contribution we did not exclude because it is lower than the $\sigma_{\rm phot}$ of the Fe XVI λ262.98 line intensities and the calibration uncertainty of the instrument. Moreover, the ratios of this blend with other strong lines of Fe XIII observable with EIS are density sensitive in the range $\log(N_{\rm e}\ [\mathrm{cm}^{-3}])$ 8.0–10.0, which corresponds to the densities of the observed structures. Therefore, the deblending of this line would be, if needed, difficult to perform. Even though the intensities of this line measured in the QS should be taken with a grain of salt, we used them as high-temperature constraints ensuring the convergence of the DEMs. To constrain DEMs at high temperatures in ARs, lines of Ca XIV–Ca XVII or Ni XVII are often used (see, e.g., Warren et al. 2012; Del Zanna 2013b; Mackovjak et al. 2014). As we were trying to avoid using lines of ions other than iron, we used the Fe XVII λ254.9 line instead. This line is weak, and we were only able to distinguish it from the continuum in spectra of M1, M2, and LC. Based on the shape of the line, it could be blended in its blue wing, even though no blend is suggested by the synthetic spectra. The blend is, however, well separated from the peak of Fe XVII, and we could fit the profile using two Gaussians. The intensities obtained were typically only a few erg cm^{-2} s^{-1} sr^{-1} in fits with $\chi^2_{\rm red}$ of the order of 10. Nevertheless, intensities of this line of this order of magnitude are comparable to those we obtained using forward modeling and were sufficient as a high-temperature constraint for our DEMs.

ORCID iDs

Juraj Lörinčík https://orcid.org/0000-0002-9690-8456
Jaroslav Dudík https://orcid.org/0000-0003-1308-7427
Giulio del Zanna https://orcid.org/0000-0002-4125-0204
Elena Dzifčáková https://orcid.org/0000-0003-2629-6201
Helen E. Mason https://orcid.org/0000-0002-6418-7914

References

Bakke, H., Frogner, L., & Gudiksen, B. V. 2018, A&A, 620, L5
Berrington, K. A., Ballance, C. P., Griffin, D. C., & Badnell, N. R. 2005, JPhB, 38, 1667
Bian, N. H., Emslie, A. G., Stackhouse, D. J., & Kontar, E. P. 2014, ApJ, 796, 142
Burge, C. A., Petkaki, P., & MacKinnon, A. L. 2012, SoPh, 280, 575
Cargill, P. J. 2014, ApJ, 784, 49
Che, H. 2018, JPhCS, 1100, 012005
Che, H., & Goldstein, M. L. 2014, ApJL, 795, L38
Christe, S., Hannah, I. G., Krucker, S., McTiernan, J., & Lin, R. P. 2008, ApJ, 677, 1385
Culhane, J. L., Harra, L. K., James, A. M., et al. 2007, SoPh, 243, 19
de Avillez, M. A., Anela, G. J., & Breitschwerdt, D. 2018, A&A, 616, A58
de Avillez, M. A., & Breitschwerdt, D. 2015, A&A, 580, A124
Delaboudinière, J. P., Artzner, G. E., Brunaud, J., et al. 1995, SoPh, 162, 291
Del Zanna, G. 2010, A&A, 514, A41
Del Zanna, G. 2011, A&A, 533, A12
Del Zanna, G. 2012, A&A, 537, A38
Del Zanna, G. 2013a, A&A, 555, A47
Del Zanna, G. 2013b, A&A, 558, A73
Del Zanna, G., & Badnell, N. R. 2014, A&A, 570, A56
Del Zanna, G., Gupta, G. R., & Mason, H. E. 2019, A&A, 631, A163
Del Zanna, G., & Mason, H. E. 2003, A&A, 406, 1089
Del Zanna, G., & Mason, H. E. 2018, LRSP, 15, 5
Del Zanna, G., O'Dwyer, B., & Mason, H. E. 2011, A&A, 535, A46
Del Zanna, G., & Storey, P. J. 2012, A&A, 543, A144
Del Zanna, G., & Storey, P. J. 2013, A&A, 549, A42
Del Zanna, G., Storey, P. J., Badnell, N. R., & Mason, H. E. 2012a, A&A, 541, A90
Del Zanna, G., Storey, P. J., Badnell, N. R., & Mason, H. E. 2012b, A&A, 543, A139
Del Zanna, G., Storey, P. J., Badnell, N. R., & Mason, H. E. 2014, A&A, 565, A77
de Pontieu, B., Berger, T. E., Schrijver, C. J., & Title, A. M. 1999, SoPh, 190, 419
de Pontieu, B., Hansteen, V. H., McIntosh, S. W., & Patsourakos, S. 2009, ApJ, 702, 1016
Dere, K. P., Del Zanna, G., Young, P. R., Landi, E., & Sutherland, R. S. 2019, ApJS, 241, 22
Dere, K. P., Doschek, G. A., Mariska, J. T., et al. 2007, PASJ, 59, S721
Dere, K. P., Landi, E., Mason, H. E., Monsignori Fossi, B. C., & Young, P. R. 1997, A&AS, 125, 149
Dudík, J., Del Zanna, G., Mason, H. E., & Dzifčáková, E. 2014, A&A, 570, A124
Dudík, J., Dzifčáková, E., Del Zanna, G., et al. 2019, A&A, 626, A88
Dudík, J., Dzifčáková, E., Meyer-Vernet, N., et al. 2017, SoPh, 292, 100
Dudík, J., Mackovjak, Š, Dzifčáková, E., et al. 2015, ApJ, 807, 123
Dudík, J., Polito, V., Dzifčáková, E., Del Zanna, G., & Testa, P. 2017, ApJ, 842, 19
Dzifčáková, E. 1992, SoPh, 140, 247
Dzifčáková, E. 2006, SoPh, 234, 243
Dzifčáková, E., & Dudík, J. 2013, ApJS, 206, 6
Dzifčáková, E., Dudík, J., Kotrč, P., Fárník, F., & Zemanová, A. 2015, ApJS, 217, 14
Dzifčáková, E., Dudík, J., & Mackovjak, Š 2016, A&A, 589, A68
Dzifčáková, E., & Kulinová, A. 2010, SoPh, 263, 25
Dzifčáková, E., & Mason, H. 2008, SoPh, 247, 301
Dzifčáková, E., Vocks, C., & Dudík, J. 2017, A&A, 603, A14
Dzifčáková, E., Zemanová, A., Dudík, J., & Mackovjak, Š 2018, ApJ, 853, 158
Fletcher, L., & De Pontieu, B. 1999, ApJL, 520, L135
Fletcher, L., Dennis, B. R., Hudson, H. S., et al. 2011, SSRv, 159, 19
Golub, L., Deluca, E., Austin, G., et al. 2007, SoPh, 243, 63
Gordovskyy, M., Browning, P. K., Kontar, E. P., & Bian, N. H. 2013, SoPh, 284, 489
Gordovskyy, M., Browning, P. K., Kontar, E. P., & Bian, N. H. 2014, A&A, 561, A72
Hannah, I. G., Christe, S., Krucker, S., et al. 2008, ApJ, 677, 704
Hannah, I. G., & Kontar, E. P. 2012, A&A, 539, A146
Hasegawa, A., Mima, K., & Duong-van, M. 1985, PhRvL, 54, 2608
Jeffrey, N. L. S., Fletcher, L., & Labrosse, N. 2016, A&A, 590, A99
Jeffrey, N. L. S., Fletcher, L., & Labrosse, N. 2017, ApJ, 836, 35
Kašparová, J., & Karlický, M. 2009, A&A, 497, L13
Klimchuk, J. A. 2006, SoPh, 234, 41
Kosugi, T., Matsuzaki, K., Sakao, T., et al. 2007, SoPh, 243, 3
Laming, J. M., & Lepri, S. T. 2007, ApJ, 660, 1642
Landi, E., Del Zanna, G., Young, P. R., Dere, K. P., & Mason, H. E. 2012, ApJ, 744, 99
Landi, E., & Feldman, U. 2003, ApJ, 592, 607
Landi, E., & Young, P. R. 2010, ApJ, 714, 636
Landi, E., Young, P. R., Dere, K. P., Del Zanna, G., & Mason, H. E. 2013, ApJ, 763, 86

Lazar, M., Fichtner, H., & Yoon, P. H. 2016, A&A, 589, A39
Le Chat, G., Issautier, K., Meyer-Vernet, N., et al. 2010, in AIP Conf. Ser. 1216, Twelfth International Solar Wind Conf., ed. M. Maksimovic et al. (Melville, NY: AIP), 316
Liang, G. Y., & Badnell, N. R. 2010, A&A, 518, A64
Liang, G. Y., Badnell, N. R., Crespo López-Urrutia, J. R., et al. 2010, ApJS, 190, 322
Liang, G. Y., Badnell, N. R., & Zhao, G. 2012, A&A, 547, A87
Liang, G. Y., Whiteford, A. D., & Badnell, N. R. 2009, A&A, 500, 1263
Lin, R. P., Schwartz, R. A., Kane, S. R., Pelling, R. M., & Hurley, K. C. 1984, ApJ, 283, 421
Livadiotis, G. 2017, Kappa Distributions: Theory and Applications in Plasmas (Amsterdam: Elsevier)
Livadiotis, G., & McComas, D. J. 2009, JGRA, 114, A11105
Ljepojevic, N. N., & MacNeice, P. 1988, SoPh, 117, 123
Mackovjak, Š, Dzifčáková, E., & Dudík, J. 2013, SoPh, 282, 263
Mackovjak, Š, Dzifčáková, E., & Dudík, J. 2014, A&A, 564, A130
Maksimovic, M., Pierrard, V., & Lemaire, J. F. 1997, A&A, 324, 725
Mariska, J. T. 2013, SoPh, 282, 629
Marsch, E. 2006, LRSP, 3, 1
Martinović, M. M., Zaslavsky, A., Maksimović, M., et al. 2016, JGRA, 121, 129
Mason, H. E., & Monsignori Fossi, B. C. 1994, A&ARv, 6, 123
Meyer-Vernet, N., Issautier, K., & Moncuquet, M. 2017, JGRA, 122, 7925
Mulay, S. M., Del Zanna, G., & Mason, H. 2017a, A&A, 598, A11
Mulay, S. M., Del Zanna, G., & Mason, H. 2017b, A&A, 606, A4
Nieves-Chinchilla, T., & Viñas, A. F. 2008, JGRA, 113, A02105
O'Dwyer, B., Del Zanna, G., Mason, H. E., et al. 2011, A&A, 525, A137
Oka, M., Birn, J., Battaglia, M., et al. 2018, SSRv, 214, 82
Oka, M., Ishikawa, S., Saint-Hilaire, P., Krucker, S., & Lin, R. P. 2013, ApJ, 764, 6
Oka, M., Krucker, S., Hudson, H. S., & Saint-Hilaire, P. 2015, ApJ, 799, 129
Olbert, S. 1968, in Summary of Experimental Results from M.I.T. Detector on IMP-1, Vol. 10, ed. R. D. L. Carovillano & J. F. McClay (Dordrecht: Springer), 641
Owocki, S. P., & Scudder, J. D. 1983, ApJ, 270, 758
Phillips, K. J. H., Feldman, U., & Landi, E. 2008, Ultraviolet and X-ray Spectroscopy of the Solar Atmosphere (Cambridge: Cambridge Univ. Press)
Pierrard, V., & Lazar, M. 2010, SoPh, 267, 153
Polito, V., Del Zanna, G., Valori, G., et al. 2017, A&A, 601, A39
Polito, V., Dudík, J., Kašparová, J., et al. 2018, ApJ, 864, 63
Priest, E. R., Chitta, L. P., & Syntelis, P. 2018, ApJL, 862, L24
Reep, J. W., Bradshaw, S. J., & Klimchuk, J. A. 2013, ApJ, 764, 193
Ripperda, B., Porth, O., Xia, C., & Keppens, R. 2017, MNRAS, 467, 3279
Roussel-Dupré, R. 1980, SoPh, 68, 243
Scherrer, P. H., Bogart, R. S., Bush, R. I., et al. 1995, SoPh, 162, 129
Scudder, J. D. 2019, ApJ, 885, 138
Scudder, J. D., & Karimabadi, H. 2013, ApJ, 770, 26
Shoub, E. C. 1983, ApJ, 266, 339
Threlfall, J., Hood, A. W., & Browning, P. K. 2018, A&A, 611, A40
Tripathi, D., Mason, H. E., Del Zanna, G., & Young, P. R. 2010, A&A, 518, A42
Tripathi, D., Mason, H. E., Dwivedi, B. N., del Zanna, G., & Young, P. R. 2009, ApJ, 694, 1256
Vasyliunas, V. M. 1968, JGR, 73, 2839
Viall, N. M., & Klimchuk, J. A. 2017, ApJ, 842, 108
Vocks, C., Dzifčáková, E., & Mann, G. 2016, A&A, 596, A41
Vocks, C., Mann, G., & Rausche, G. 2008, A&A, 480, 527
Wannawichian, S., Ruffolo, D., & Kartavykh, Y. Y. 2003, ApJS, 146, 443
Warren, H. P., & Brooks, D. H. 2009, ApJ, 700, 762
Warren, H. P., Ugarte-Urra, I., & Landi, E. 2014, ApJS, 213, 11
Warren, H. P., Winebarger, A. R., & Brooks, D. H. 2012, ApJ, 759, 141
Warren, H. P., Winebarger, A. R., Mariska, J. T., Doschek, G. A., & Hara, H. 2008, ApJ, 677, 1395
Watanabe, T., Hara, H., Yamamoto, N., et al. 2009, ApJ, 692, 1294
Woods, T. N., Eparvier, F. G., Hock, R., et al. 2012, SoPh, 275, 115
Wright, P. J., Hannah, I. G., Grefenstette, B. W., et al. 2017, ApJ, 844, 132
Young, P. R., Del Zanna, G., Mason, H. E., et al. 2007, PASJ, 59, S857
Young, P. R., Watanabe, T., Hara, H., & Mariska, J. T. 2009, A&A, 495, 587